Optimal North Pacific Blocking Precursors and Their Deterministic Subseasonal Evolution during Boreal Winter

MELISSA L. BREEDEN

Chemical Sciences Division, NOAA/Earth System Research Laboratory, Boulder, Colorado

BRETT T. HOOVER

Cooperative Institute for Meteorological and Satellite Studies, University of Wisconsin–Madison, Madison, Wisconsin

MATTHEW NEWMAN

Physical Sciences Division, NOAA/Earth System Research Laboratory, and Cooperative Institute for Research in Environmental Sciences, University of Colorado Boulder, Boulder, Colorado

DANIEL J. VIMONT

Department of Atmospheric and Oceanic Sciences, University of Wisconsin–Madison, Wisconsin, Madison

(Manuscript received 21 August 2019, in final form 15 November 2019)

ABSTRACT

Atmospheric blocking is associated with sensible weather impacts such as anomalous precipitation and flooding, cold air outbreaks, and heat waves. Given the asymmetry in the persistence characteristics of anticyclones and cyclones, many studies have emphasized the role of nonlinearities in blocking onset and maintenance. However, previous studies have demonstrated that both linear and nonlinear dynamics can amplify blocks. In this paper the structure and evolution of North Pacific blocking on weekly time scales is investigated using two methods: statistical analysis not requiring linearity, and a linear inverse model (LIM) composed of tropical outgoing longwave radiation and extratropical streamfunction, which relies on purely linear (and linearly parameterized) dynamics. Both approaches produce a similar evolution of North Pacific blocking. Using the LIM, the optimal precursors to blocking are determined, which at a 14-day lead time include an upper-level east Pacific anticyclone and suppressed convection over the central tropical Pacific. The tropics and extratropics both contribute to the deterministic evolution of blocking, with the tropics acting on longer time scales but imposing a weaker response than that contributed by the extratropics. The tropical contribution was driven by La Niña–like conditions that produce a hemispheric anticyclonic anomaly, while the extratropical initial conditions produce an equivalent barotropic, wavelike pattern. The LIM's ability to reproduce the observed blocking evolution suggests the predictable evolution of blocking on weekly time scales can be modeled in a linear framework, and that subseasonal forecasting of North Pacific blocking needs to consider both tropical and extratropical conditions.

1. Introduction

Atmospheric blocking is defined by prolonged periods during which the storm track is diverted around a persistent, large-scale anticyclone. Often accompanied by cyclones to the south (Rex or dipole-type block) or flanking it on either side (omega block), blocks dramatically modify the regional precipitation and temperature by altering not only the atmospheric flow over the blocking region but upstream and downstream as well (Berggren et al. 1949; Rex 1950; Carrera et al. 2004; Röthlisberger et al. 2016; Winters et al. 2019). Blocks can last for 1–3 weeks, and are associated with anomalous storm tracks, extreme wintertime temperatures, and flooding (Carrera et al. 2004; Lau and Kim 2012) as well as summertime heat waves (Campetella and Rusticucci 1998; Matsueda 2011; Parker et al. 2014)

Corresponding author: Melissa L. Breeden, melissa.breeden@noaa.gov

DOI: 10.1175/MWR-D-19-0273.1

through subsidence warming of the troposphere, sustained solar insolation, and land surface feedbacks (Dole et al. 2011).

Numerous studies have focused on the mechanisms driving the initiation and maintenance of blocks, often framed in terms of the relative importance of linear and nonlinear processes. Nonlinear processes can produce a feedback onto the low-frequency circulation to maintain a block (Shutts 1983; Hoskins et al. 1983), and might preferentially reinforce anticyclones compared to cyclones (Dole and Gordon 1983; Yamazaki and Itoh 2013). However, Sardeshmukh et al. (2015) showed that the asymmetry in persistence characteristics of anticyclonic versus cyclonic anomalies, first explored by Dole and Gordon (1983), can be reproduced through a linear system forced by correlated additive-multiplicative noise. That is, the *predictable* evolution of blocks may be essentially linear even if nonlinear processes are large, when the nonlinear processes have a much shorter time scale than the linear processes. Furthermore, linear processes, such as linear baroclinic and barotropic amplification, have been demonstrated to amplify North Pacific blocks (Breeden and Martin 2018), while North Atlantic blocks were found to be substantially driven by nonlinear processes (Evans and Black 2003).

On weekly and monthly time scales, teleconnection patterns, in which circulation anomalies over a vast region vary in tandem, can also affect North Pacific blocking frequency. The state of El Niño–Southern Oscillation (ENSO) as well as the phase of the Madden–Julian oscillation (MJO) have been shown to affect North Pacific blocking frequency (Renwick and Wallace 1996; Henderson et al. 2016). Renwick and Wallace (1996) found that North Pacific blocking occurred more often during winters characterized by the negative phase of the Pacific–North American pattern, which can develop from internal atmospheric variability (PNA; Wallace and Gutzler 1981; Cash and Lee 2001). Henderson et al. (2017) used a linear baroclinic model to demonstrate that MJO teleconnections can be modeled as linear processes in the Pacific. It therefore appears that blocks developing in the North Pacific and North Atlantic may be driven by linear and nonlinear processes in different proportions. North Pacific blocks, in particular, appear to be heavily influenced by linear processes including teleconnection patterns and linear baroclinic and barotropic amplification. We therefore hypothesize that a linear model could capture the development of blocks on weekly time scales.

A tangent linear modeling framework has been used to diagnose the optimal initial conditions that evolve to produce a block within the next few days (Frederiksen 1998; Mu and Jiang 2008). For lead times longer than several days, however, the assumptions made in a tangent linear approach do not hold. In this study, we develop a linear stochastic model in which, with suitable averaging, a nonlinear dynamical system can be approximated by the dynamics of a stable, linear system forced by stochastic white noise. This method allows for examination of the optimal precursors to blocking on time scales markedly longer than those attainable through a tangent linear model approach. Penland and Sardeshmukh (1995) introduced a framework for determining such a linear system from observations, by constructing a linear inverse model (LIM), where the dynamics of the system are inferred from the lagged covariance of a reduced space system state. That study demonstrated that, despite the requirement that the dynamics of the system be damped in the long-term, monthly mean tropical sea surface temperature anomalies could grow via nonnormal modal interference for as long as 15 months (note that the nonnormal growth process is a direct result of the nonorthogonality of the system eigenmodes and should be distinguished from modal growth that might arise from linear instability of a system eigenmode; Farrell and Ioannou 1993). Nonnormal growth is also a characteristic of realistic geophysical systems with location-dependent linear dynamics, such as might result from shear and from boundary-driven diabatic/dissipative processes (Farrell 1984; Barcilon and Bishop 1998). Previous studies have constructed LIMs to model Northern Hemisphere atmospheric variability and investigated the most rapidly growing structures that develop via nonnormal interactions on daily and weekly time scales, without any constraint on the final patterns that the models produced (Cash and Lee 2001; Winkler et al. 2001).

A LIM can also be used to optimize growth toward a prescribed circulation pattern, such as North Pacific blocking. In that case, growth is defined using a specified norm that represents the phenomenon of interest (Zanna and Tziperman 2005). Vimont (2012) and Vimont et al. (2014) used a LIM with specified norms to identify optimal growth of the Atlantic meridional mode (Chiang and Vimont 2004) and central versus east Pacific ENSO variability. The present study introduces a new application of the LIM, in which, using a LIM similar to that developed by Winkler et al. (2001), we optimize growth associated with the phenomenon of North Pacific blocking. Through the LIM approach the *predictable* and *linear* evolution of North Pacific blocking on subseasonal time scales is investigated. In addition to optimizing growth in a given pattern of interest, we can isolate specific interactions within the model, such as the impact of tropical heating on the extratropical streamfunction and vice

versa. In this manner the relative contributions to North Pacific blocking from the tropics and extratropics are considered, to compare to previous studies that have emphasized the role of teleconnection patterns from the tropics and extratropics in North Pacific block development.

The intent of this study is to briefly characterize the structure and evolution of North Pacific blocking events, and determine whether that structure and evolution can be reproduced within a LIM framework. This paper is organized as follows. Section 2 describes the data used in this study and the LIM methodology. In section 3 the characteristics of North Pacific blocking events are described using statistical techniques that do not assume linearity. In section 4, the approach used to define the blocking norm is described and used to investigate the optimal initial conditions that amplify into a North Pacific block. The relative influences of tropical heating and extratropical streamfunction in producing blocking are described as well. Section 5 examines the dependence of the tropical and extratropical contributions to blocking on optimization lead time. Section 6 concludes with a discussion of the implications of the results for the predictability of blocking at subseasonal time scales.

2. Data and methods

a. Data

Daily mean zonal and meridional wind at 200 and 850 hPa from the National Centers for Environmental Prediction–National Center for Atmospheric Research (NCEP–NCAR) Reanalysis I dataset were interpolated to 2° × 2° spatial resolution (Kalnay et al. 1996), and then smoothed with a 7-day running mean. A daily climatology from 1980 to 2014 was determined from each 7-day running mean field as the time-mean plus the first four harmonics of the annual cycle, and anomalies were then calculated as departures from this climatology. Streamfunction anomalies were then calculated from these global wind anomalies using SPHEREPACK routines available through NCAR (Adams and Swarztrauber 1997). For the blocking criteria discussed in section 3, the streamfunction anomalies were standardized with respect to the December–February 1980–2014 standard deviation at each grid point. Outgoing longwave radiation (OLR) was obtained from the National Oceanic and Atmospheric Administration (NOAA) daily interpolated dataset (Liebmann and Smith 1996), and anomalies were computed in the same manner as the streamfunction. OLR anomalies were not used in the blocking criteria.

b. Linear inverse model

The evolution of a system state x can be expressed as follows:

$$\frac{d\mathbf{x}}{dt} = \mathbf{B}\mathbf{x} + N(\mathbf{x}), \tag{1}$$

where $\mathbf{x}$ is the system state vector, $\mathbf{B}$ is the linearized component of the dynamical equations, and $N(\mathbf{x})$ represents the nonlinear component. Here, we assume that $\mathbf{x}$ is defined as the deviation with respect to some climatological average $\mathbf{x} = \mathbf{X} - \bar{\mathbf{x}}$, where the climatological average is taken over a time interval appropriate for the component of the state vector (e.g., monthly averages of sea surface temperature, and averages of several days to a week for components of the atmosphere). To the extent that the critical nonlinearities represented by $N(\mathbf{x})$ operate on time scales that are short compared to the linear dynamics described by $\mathbf{B}\mathbf{x}$, it is often possible to approximate the nonlinear terms as a *second* linear operator acting on the state variable plus temporally (although not spatially) incoherent noise, yielding the linear model:

$$\frac{d\mathbf{x}}{dt} = \mathbf{L}\mathbf{x} + \mathbf{F}_s \tag{2}$$

(Penland and Sardeshmukh 1995). We emphasize that $\mathbf{L}$ can include linearized dynamics *and* a linear approximation of nonlinearities, and $\mathbf{F}_s$ represents white noise forcing.

A linear inverse model (LIM) is an empirical model inferring the linear dynamics of a system governed by (2) from its lagged covariance statistics; that is, a LIM estimates $\mathbf{L}$ and the covariance of the noise forcing from observations. When approximating (1) by (2), $\mathbf{F}_s$ may include a linear (''multiplicative'') dependence upon the state $\mathbf{x}$, allowing (2) to generate non-Gaussian variability and asymmetry in the duration of opposite-signed events, even as the predictable component reflects only linear dynamics (see Sardeshmukh et al. 2015). However, here we limit $\mathbf{F}_s$ to represent only state-independent (''additive'') noise, which makes using LIM to determine (2) from limited observations more tractable (but see Martinez Villalobos et al. 2018).

Solving the homogeneous system from (2) yields

$$\mathbf{x}(t+\tau) = \exp(\mathbf{L}\tau)\mathbf{x}(t) \equiv \mathbf{G}_\tau \mathbf{x}(t). \tag{3}$$

For a given choice of lag $\tau = \tau_0$, $\mathbf{G}_{\tau_o}$ can be determined using the covariance matrices of the system state $\mathbf{x}$ at lags of zero and τ_o days, represented by $\mathbf{C}_0$ and $\mathbf{C}_{\tau_o}$, respectively:

$$\mathbf{G}_{\tau_o} = \mathbf{C}_{\tau_o}\mathbf{C}_o^{-1}. \quad (4)$$

The dynamical system operator $\mathbf{L}$ is then determined from the matrix logarithm of $\mathbf{G}_{\tau_o}$:

$$\mathbf{L} = \ln\left(\mathbf{G}_{\tau_o}\right)\Big/\tau_o. \quad (5)$$

In a perfectly linear system the model would be insensitive to τ_o, an assumption that can be tested (appendix A, Fig. A1; see Penland and Sardeshmukh 1995 for further explanation). A τ_o of five days lies within the range where this approximation is reasonable and is used in the present study to define a single $\mathbf{L}$ from (5), as done in Winkler et al. 2001. An ensemble-mean LIM forecast is then computed for any chosen lead time τ from (3), assuming the subsequent predictable evolution of $\mathbf{x}$ remains sufficiently represented as a linear, stable system.

The state vector for the LIM used here is

$$\mathbf{x} = [\mathrm{OLR}\ \Psi_{850}\ \Psi_{200}]. \quad (6)$$

Empirical orthogonal function (EOF) analysis was applied to each variable, individually, to reduce the dimensions of the state vector. The EOF domain for OLR anomalies was 20°S–20°N, and for 850 and 200 hPa streamfunction anomalies (Ψ_{850} and Ψ_{200} was 20°–90°N. All three variables are global in longitude. We retained 85% of the total variance at each vertical (pressure) level, corresponding to 18 EOFs of Ψ_{200} and 16 EOFs of Ψ_{850}. The 20 leading OLR EOFs were retained, explaining 53% of the total tropical OLR variance; each additional EOF contributed less than 1% to the total variance, suggesting they are not crucial to understanding predictable large-scale OLR variability. Thus, $\mathbf{x}$ represents the corresponding principal components (PCs) of the retained EOFs. In the appendix it is shown that the LIM constructed here is stable, and the system described by the state vector is sufficiently linear, a requirement for successful use of a LIM as outlined by Penland and Sardeshmukh (1995).

Anomaly amplification is possible when the eigenvectors of $\mathbf{L}$ are nonorthogonal. Transient, finite-amplitude system growth can then arise through destructive or constructive interference between the eigenvectors (Penland and Sardeshmukh 1995). This condition of nonorthogonality is satisfied, for example, in the presence of shear and zonal asymmetry in the flow, which are both characteristic of the strong boreal winter North Pacific jet (e.g., Borges and Sardeshmukh 1995). The amount of growth achieved through such nonnormal interactions varies with growth period, or lead time. Farrell (1988) showed that such transient growth $\mu(\tau)$ over a specified lead time τ may be calculated as follows:

$$\mu(\tau) = \frac{\mathbf{x}(\tau)^{\mathrm{T}}\mathbf{N}\mathbf{x}(\tau)}{\mathbf{x}(0)^{\mathrm{T}}\mathbf{D}\mathbf{x}(0)} = \frac{\mathbf{x}(0)\mathbf{G}(\tau)^{\mathrm{T}}\mathbf{N}\mathbf{G}(\tau)\mathbf{x}(0)}{\mathbf{x}(0)^{\mathrm{T}}\mathbf{D}\mathbf{x}(0)}, \quad (7)$$

where $\mathbf{D}$ and $\mathbf{N}$ represent the initial and final norm kernels, respectively. In this study, we do not specify anything about the initial conditions that maximize growth, so $\mathbf{D}$ is the identity matrix. The final norm kernel can be a measure of the direction in which growth is maximized. Initial structures optimizing anomaly growth in the direction of the final norm are determined from the corresponding eigenvalue problem (Farrell 1988; Penland and Sardeshmukh 1995; Tziperman and Ioannou 2002). Under the Euclidean, or "L2" norm, $\mathbf{N}$ is also the identity matrix, in which case the initial structure that maximizes global growth over the time interval τ is determined from

$$[\mathbf{G}(\tau)^{\mathrm{T}}\mathbf{G}(\tau)]\mathbf{v}(\tau) = \mu(\tau)\mathbf{v}(\tau), \quad (8)$$

where $\mu(\tau)$ is the amplification of the domain integrated variance of $\mathbf{x}$. These structures were examined by Winkler et al. (2001) for a similar LIM as the one used here. To instead find maximum amplification of a specified spatial structure, different final norms must be used. Here, to focus on growth of North Pacific blocks, we determined and implemented a final blocking norm $\mathbf{N}$, and solved the generalized eigenvalue problem:

$$[\mathbf{G}(\tau)^{\mathrm{T}}\mathbf{N}\mathbf{G}(\tau)]\mathbf{v}(\tau) = \mu(\tau)\mathbf{v}(\tau). \quad (9)$$

Thus, given knowledge of the deterministic dynamics of the system from $\mathbf{G}(\tau)$ and specification of the final norm $\mathbf{N}$, the initial optimal pattern $\mathbf{v}(\tau)$ that maximizes growth $\mu(\tau)$ can be assessed by computing the eigendecomposition of $\mathbf{G}(\tau)$ under $\mathbf{N}$. [The more general singular value decomposition technique can also be used to determine the optimal initial structures as done in Winkler et al. 2001]. Each eigenvector now corresponds to the initial condition producing growth measured by $\mathbf{N}$, with amplitude eigenvalue $\mu(\tau)$ for a specific lead time τ. The eigenvector corresponding to the largest eigenvalue, which produces the strongest growth given $\mathbf{N}$, is referred to as the *optimal initial structure* (Farrell 1988; Vimont 2012). Note that, for the final blocking norm specified in this study, $\mu(\tau)$ measures amplification from a unit amplitude of $\mathbf{x}$ in the direction of the initial norm that is potentially spread across all system components, into the direction of the final norm only, and as such does not equally measure change in all system components.

An explanation of how the norm used in this study was defined is presented in section 4a.

3. Evolution of North Pacific blocks

In this section, the structure and evolution of North Pacific blocking events are described, with the intent of providing a baseline against which the LIM-simulated block evolution can be compared. Section 3a describes the method used for identifying blocks, and section 3b describes the structure and evolution of North Pacific blocking events using composite analysis.

a. Identifying North Pacific blocking events

There are several methods used to identify atmospheric blocking in the extratropics, including tracking persistent anticyclones in a fixed geographic area (Dole and Gordon 1983) and searching for a meridional reversal in the geopotential height or potential temperature gradient (Tibaldi and Molteni 1990; Pelly and Hoskins 2003). Barnes et al. (2012) compared three identification methods, based on reversals in 500 hPa geopotential height, potential temperature on the 2 PVU (1 PVU $= 10^{-6}\,\mathrm{K\,kg^{-1}\,m^2\,s^{-1}}$) surface ($\theta_2$), and 500 hPa zonal wind, finding general agreement in blocking frequency for the majority of the Northern Hemisphere except in the Pacific region, where the θ_2 approach underestimated block frequency compared to the other two metrics.

In this study, we adopt a Dole and Gordon (1983) approach to blocking, which is tailored to identify persistent, North Pacific wintertime anticyclones and allows definition of blocking events based upon the streamfunction anomalies in the LIM state vector. During the 35 boreal winters (December–February), 1980–2014, blocking events were identified as occurring when the 200 hPa standardized streamfunction anomalies, averaged within the region bounded by 46°–56°N, 186°–206°E (where most frequent persistent anticyclonic anomalies occur; Miller et al. 2020; Dole and Gordon 1983), exceeded 1.25 standard deviations for at least five days. Over the 35 winters, 25 independent cases and 338 days were identified, or 10.7% of all days. This blocking frequency is generally consistent with previous measures of extratropical blocking at this longitude (Pelly and Hoskins 2003). Onset dates and durations are in Table 1, showing a wide range of block duration from 6 to 29 days, with about one-third of events persisting beyond two weeks.

Anticyclonic anomalies are more persistent than their cyclonic counterparts, which Dole and Gordon (1983) showed was due, in part, to cyclonic anomalies being more easily interrupted by transient disturbances associated with an invigorated storm track. Even after low-pass-filtering height anomalies to remove the transient behavior, however, at weak magnitudes and a duration longer than 15 days, anticyclonic anomalies were more common than cyclonic anomalies. Dole and Gordon attributed this amplitude and duration asymmetry to nonlinear processes, but Sardeshmukh et al. (2015) demonstrated that these nonlinear processes might be well approximated by a system similar to (2), but where the noise is non-Gaussian and has a linear dependence upon $\mathbf{x}$. Still, Sardeshmukh et al. (2015) showed that, at anomaly values between 1.4 and 1.7 standard deviations, negative and positive 250 hPa relative vorticity anomalies were approximately equally distributed. Thus while there are important processes that can lead to asymmetry between cyclones and anticyclones, their effects vary according to the strength of the block. The 1.25 standard deviation blocking amplitude threshold chosen in this study is near the value at which anomalies are observed to occur in roughly equivalent proportions, so we choose to defer analysis of blocking duration asymmetry to future work.

TABLE 1. Dates and duration of the blocking events used to construct norm.

Date of block onset	Duration (days)
17 Jan 1982	6
2 Feb 1982	10
20 Dec 1983	9
14 Jan 1984	8
12 Dec 1984	18
1 Feb 1985	8
25 Dec 1988	6
31 Jan 1989	29
15 Dec 1990	17
23 Jan 1991	6
17 Dec 1992	28
12 Feb 1994	8
21 Jan 1996	11
16 Feb 1996	11
19 Dec 1998	8
12 Jan 2000	12
24 Dec 2004	18
20 Feb 2007	7
21 Jan 2008	7
14 Dec 2008	15
14 Feb 2009	15
15 Dec 2010	10
13 Feb 2011	16
11 Dec 2012	6
1 Dec 2013	6

b. North Pacific blocking characteristics

The composite weekly evolution of 200 and 850 hPa streamfunction and tropical OLR anomalies, with Day_b 0 representing the first day the blocking criteria were

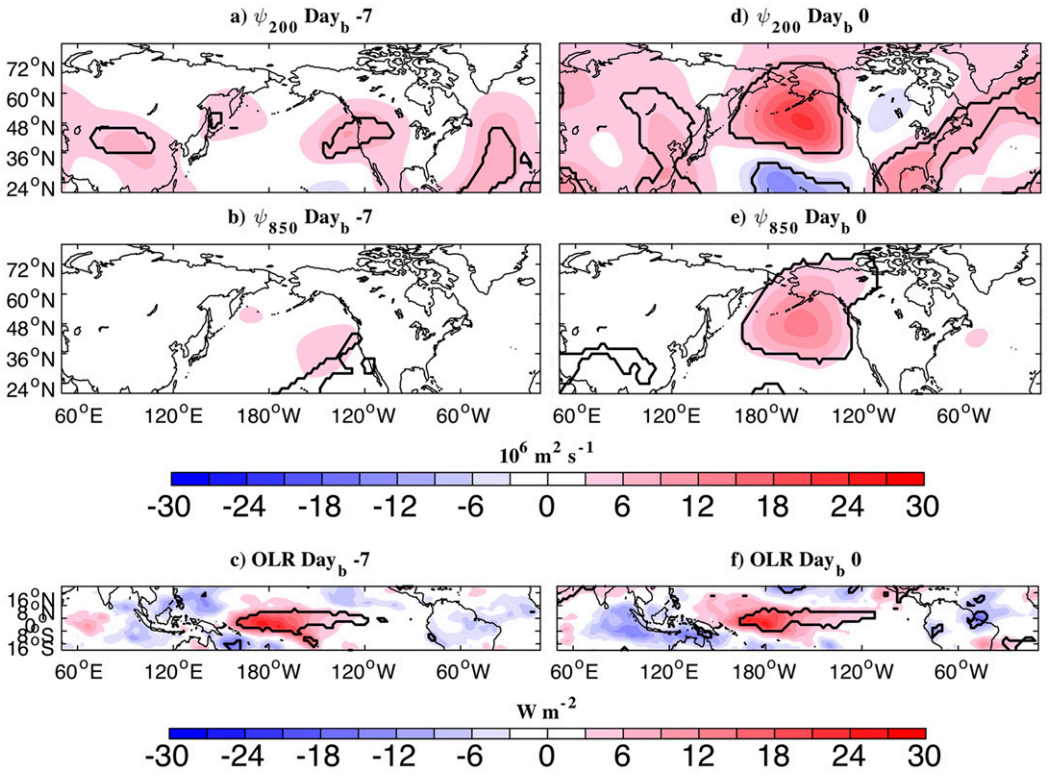

FIG. 1. Composite evolution of 200 and 850 hPa 7-day boxcar averaged streamfunction (ψ) anomalies and OLR anomalies, (a)–(c) seven days prior to block onset (Day$_b$ −7) and (d)–(f) at block onset (Day$_b$ 0). The black contours indicate areas where the composite pattern is significant at the 99% level using a two-tailed Student's t test. Units are 10^6 m^2 s^{-1} for the streamfunction patterns and W m^{-2} for the OLR patterns.

met, is shown in Fig. 1 (Day$_b$ −7 and Day$_b$ 0) and Fig. 2 (Day$_b$ +7 and Day$_b$ +14). Features significant at the 99% confidence level were determined using a two-tailed Student's t test that did not assume equal variance between samples and reduced the degrees of freedom in regions where the variance in the blocked cases and variance of the full data record was substantially different.

One week prior to central Pacific blocking onset (Day$_b$ −7), weak anticyclonic anomalies were observed in the east Pacific near 45°N, 120°W at both 850 and 200 hPa, with a second upper-level anticyclonic anomaly near the Tibetan Plateau at 45°N, 80°–100°E (Figs. 1a,b). A broad region of suppressed convection (positive OLR anomaly) was located in the central tropical Pacific (Fig. 1c). At block onset, a potent, equivalent barotropic anticyclonic anomaly developed south of Alaska (Figs. 1d,e), with an upper-level cyclonic subtropical anomaly to its south, reflective of the Rex or dipole-type block that our blocking definition captures. The suppressed tropical convection observed one week prior to block onset persisted (Fig. 1f).

Over the following week, the North Pacific upper-level anticyclone underwent continued intensification, also expanding westward, while the cyclonic subtropical anomaly slightly weakened (Fig. 2a). At 850 hPa, a cyclonic anomaly developed to the west of Hawaii, which often coincides with enhanced Hawaiian precipitation (consistent with the enhanced frequency of ''Kona lows'' that develop during blocks, Otkin and Martin 2004), confirmed by negative OLR anomalies developing to the east (Figs. 2b,c). Downstream of the block, a trough developed over western North America (at 45°N) and a ridge over the southeastern United States (at 30°N). At Day$_b$ +14, the block weakened and continued to retrograde westward, but was still significant despite the difference in the longevity of the individual blocking events (Figs. 2d,e). The cyclonic anomalies over the subtropics and North America weakened as well, while the 200 hPa anticyclone over the eastern United States persisted and remained significant. Suppressed convection in the central tropical Pacific still remained, while enhanced convection over the Maritime Continent strengthened (Fig. 2f).

The quadrupole pattern arcing from the central Pacific to cross North America at Day$_b$ 0 and Day$_b$ +7 strongly resembles the negative phase of the PNA

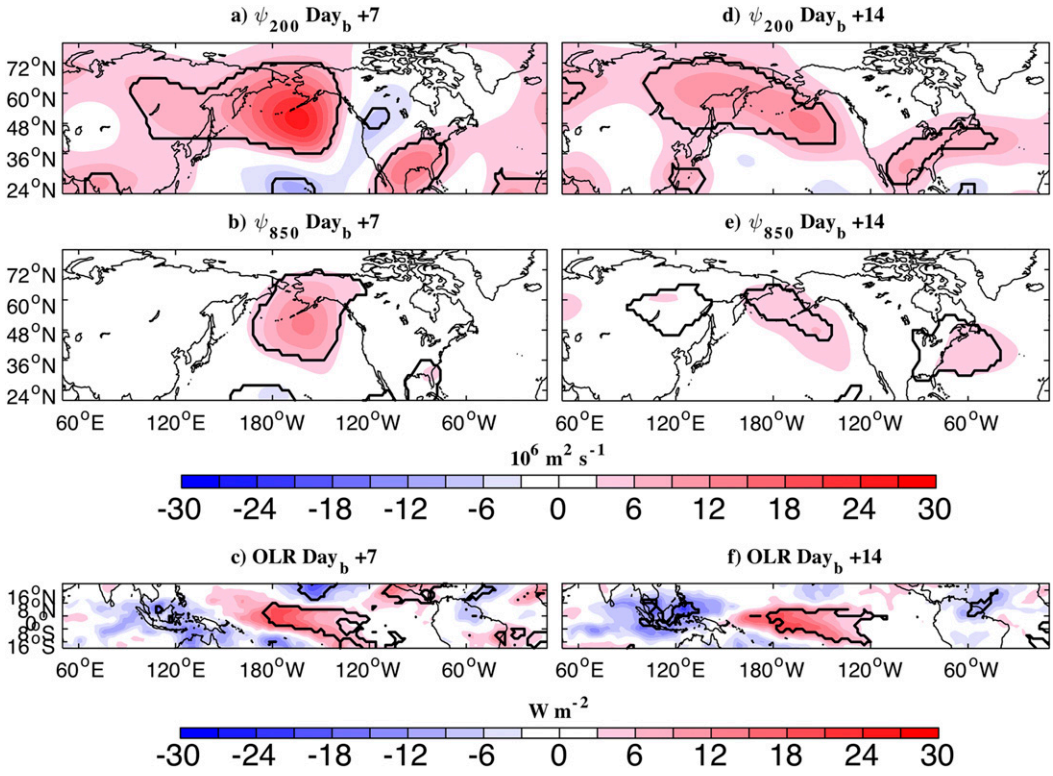

FIG. 2. As in Fig. 1, but averaged for (a)–(c) seven days following block onset (Day$_b$ +7) and (d)–(f) fourteen days following block onset (Day$_b$ +14).

(Wallace and Gutzler 1981; Barnston and Livezey 1987), with some differences in details involving the relative amplitudes and positioning of anomaly centers, especially downstream (cf. Fig. C1b). To test whether our blocking criteria have merely reproduced the PNA pattern, a blocking index was computed by projecting the composite Day$_b$ 0 200/850 hPa streamfunction pattern onto the 35-yr record of the 200/850 hPa streamfunction anomalies, respectively. Correlating this time series and the second principal component of Ψ_{200}, essentially a time series of the PNA pattern (Fig. C1b), is 0.61, indicates that the PNA, although contributing to blocking (e.g., Renwick and Wallace 1996), explains only about one-third of central Pacific blocking variability. Additionally, the temporal evolution of blocking is not simply due to ENSO: the blocking index is correlated at a value of only −0.48 with the first PC of tropical OLR, which captures ENSO temporal evolution (the negative correlation indicates that La Niña conditions correspond to blocks).

Our blocking composite also captures a key sensible weather impact of North Pacific blocking, namely, widespread cooling over North America, as found by previous studies. Figure 3 shows 2-m temperature anomaly composites before and during blocking. The region of positive OLR anomalies in the tropics was accompanied by slightly cooler temperatures near the surface, suggestive of La Niña (Fig. 3a). A warm/cold anomaly dipole from the Bering Strait and to western North America developed and persisted downstream of the block through Day$_b$ +14 (Figs. 3a–c; see also Carrera et al. 2004 Fig. 7).

A blocking index time series (Fig. 4), defined by projecting each day's 200/850 hPa streamfunction composite pattern onto the 200/850 hPa streamfunction Day$_b$ 0 composite blocking pattern (using only the North Pacific anomalies in Figs. 1d,e), shows that the composite block rapidly intensifies for about 10 days, from Day$_b$ −7 through its peak on Day$_b$ +3, followed by relatively more gradual decay from Day$_b$ +3 to Day$_b$ +15. Daily Hovmöllers of extratropical anomalies (Figs. 5a,b) show that just prior to blocking onset, the initial 200 hPa anticyclonic anomaly retrograded westward while the 850 hPa anticyclone developing beneath it did not (Fig. 5b). This retrogression is consistent with Shutts (1983), who suggested that deformation upstream of blocks can aid in their maintenance and retrogression. The equivalent barotropic structure of the resulting block, as well as its persistence from Day$_b$

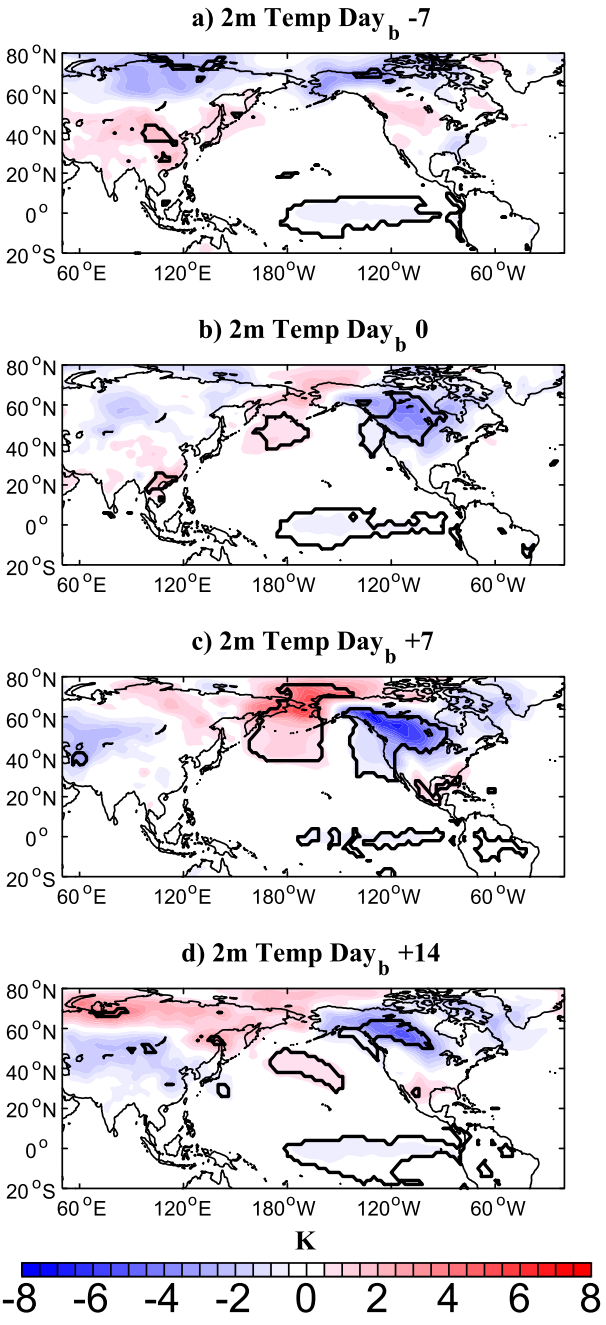

FIG. 3. Composite evolution of 2-m temperature anomalies (a) seven days prior to block onset through (d) fourteen days following block onset. Note that this plot extends to 20°S, compared to a southern limit of 0° in Figs. 1 and 2.

0 through Day$_b$ +10, confirms that our composite captures key characteristics of blocking. Positive OLR anomalies from about 160°E–170°W were observed to undergo little change throughout the time period (Fig. 5c), while weakly negative OLR anomalies from 100° to 140°E began to strengthen about five days after blocking onset, reaching peak strength at about Day$_c$ +14.

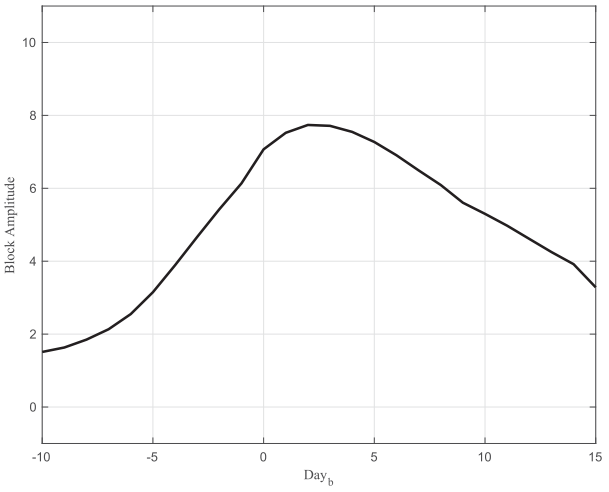

FIG. 4. Time series of the 25-event composite block amplitude beginning 10 days prior to block onset through 15 days following block onset.

4. Growth and optimal structures under blocking norms

a. *Defining a blocking norm*

Given that our blocking definition captures the essential features of North Pacific blocks, we use it to define the final blocking norm **N** [see (7) and (9)] by projecting the Day$_b$ 0 composite 200 and 850 hPa streamfunction anomaly over the North Pacific (Figs. 6a,b, with anomalies outside of the blocking region set to zero) into the LIM state space (Figs. 6c,d). For the two streamfunction components of **x**, the projection of the composite onto the retained EOFs yields two vectors ($\mathbf{r}_{\Psi_{850}}$ and $\mathbf{r}_{\Psi_{200}}$) that are inserted into a norm vector **n** in the LIM state space:

$$\mathbf{n} = \left[000 \cdots \mathbf{r}_{\Psi_{850}} \mathbf{r}_{\Psi_{200}}\right], \tag{10}$$

where the zeros indicate the OLR component of the state space (i.e., the final norm places no weight on development of OLR). The vector **n** is then normalized to unit length and is used to create the final norm **N** kernel via:

$$\mathbf{N} = \mathbf{n}^{\mathrm{T}}\mathbf{n} + \epsilon\mathbf{I}, \tag{11}$$

where a small number ϵ (we use 10^{-9}) is added to the diagonal for numerical stability.

The pattern that results from projecting the dipole pattern onto the EOFs of the state vector, plotted in Figs. 6c and 6d, at 200 hPa is associated with weak anomalies outside of the blocking region, including an elongated structure over the Pacific and eastern Asia, a trough/ridge pattern over North America, and weak anomalies over the Atlantic and Europe; these features

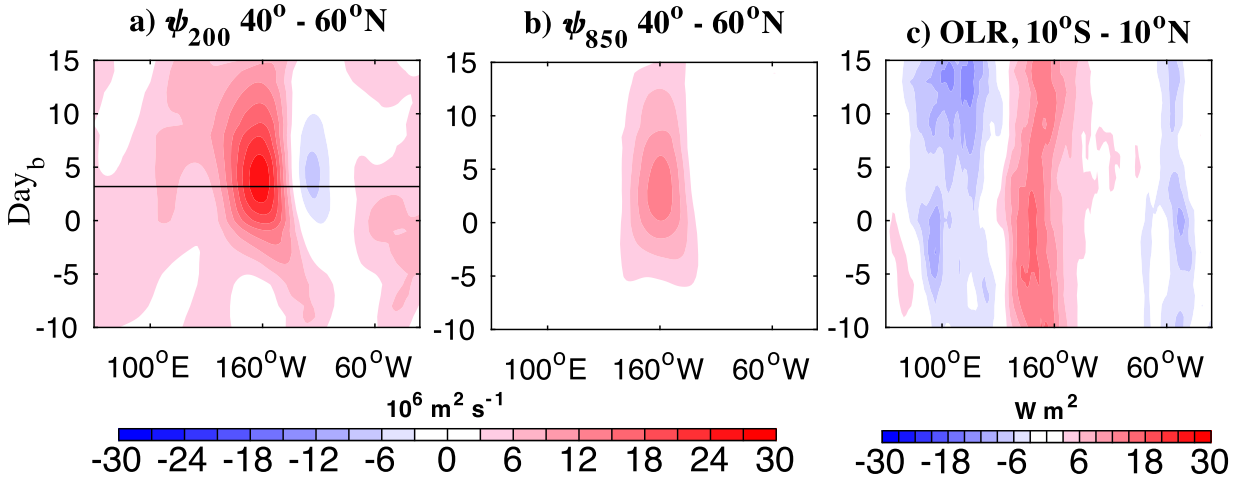

FIG. 5. Hovmöller diagrams of (a) 200 hPa streamfunction, (b) 850 hPa streamfunction, and (c) tropical OLR, beginning ten days prior to blocking onset through 15 days after block onset. The streamfunction anomalies are averaged from 40° to 60°N, and the OLR anomalies are averaged from 10°S to 10°N. The black solid line in (a) marks the time of peak block strength as indicated by Fig. 4.

are similar to those observed in the Day_b 0 composite (Fig. 1d). At 850 hPa, the blocking norm includes weaker nonlocal structure than that observed at 200 hPa. Recall that the OLR component of **N** was set to zero, so that the norm represents only growth of the block in the 200 and 850 hPa streamfunction anomalies, and does not measure the associated tropical OLR anomaly evolution.

b. *Growth and evolution of North Pacific blocks in the LIM*

Optimal (deterministic) growth under the blocking norm calculated using (7) is greatest over a 10-day interval, consistent with the observed composite (e.g., Fig. 4), although amplification can occur over periods as long as about 28 days (Fig. 7). This section will focus on the structure and behavior of the 14-day optimal initial structure, since this time interval was near peak blocking growth and outside the reliable range of NWP models. Figures 8a–c show that the optimal initial structure in the LIM's ''14-day optimal'', or the initial anomaly leading to maximum amplification of a central Pacific blocking pattern 14 days later, strongly resembles the composite anomalies preceding blocking onset (Day_b −7 in Figs. 1a–c). The optimal 200 hPa

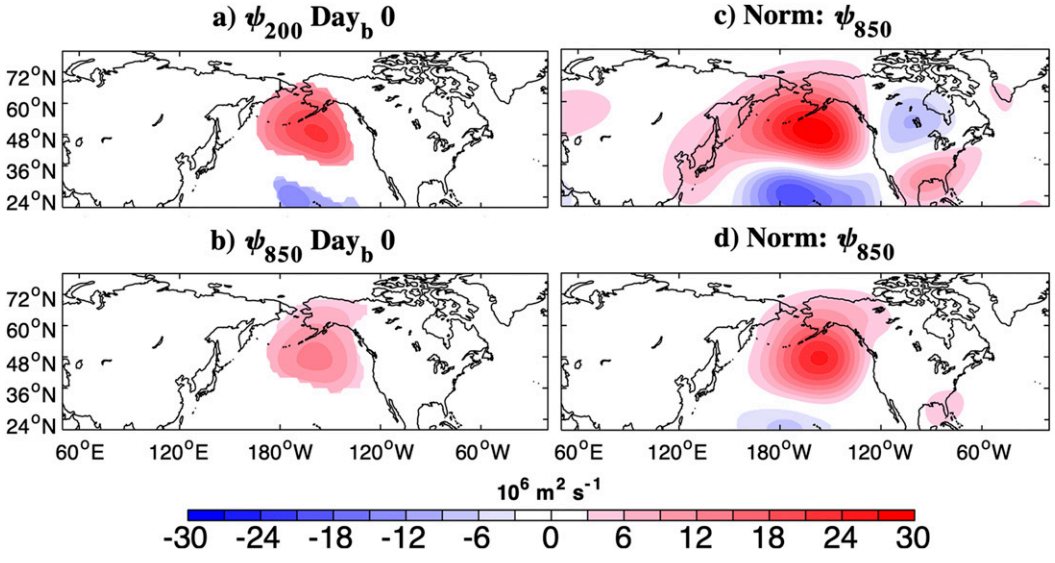

FIG. 6. Composite Day_b 0 streamfunction anomalies at (a) 200 hPa and (b) 850 hPa using the total [that is, non-EOF-truncated] streamfunction fields as in Figs. 1d and 1e. (c) 200 hPa and (d) 850 hPa streamfunction patterns projected into the EOF subspace of the LIM, which is used to create the blocking norm, **N**.

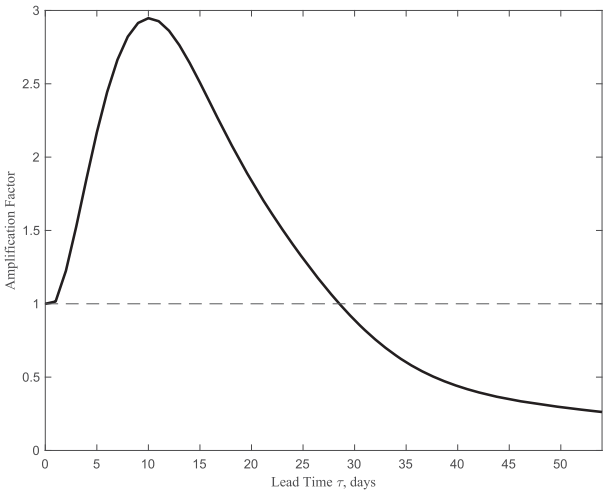

FIG. 7. Maximum system growth, as a function of optimization lead time, for the leading singular value under the blocking norm.

streamfunction anomalies include an east Pacific anticyclone in the extratropics lying to the north of a smaller-scale trough east of Hawaii (Fig. 8a), and a downstream wave train–like feature with negative anomalies over eastern North America and positive anomalies over the Atlantic. The 14-day optimal also includes a dipole structure of 200 hPa streamfunction anomalies over eastern Eurasia which contrasts with positive anomalies near the same region in the Day_b −7 composite. The 14-day optimal 850 hPa pattern has less structure overall, but in some regions has anomalies opposite to that observed at 200 hPa, including an anticyclonic anomaly beneath the 200 hPa cyclonic feature in the east Pacific (this feature is shared with the Day_b −7 composite) and a cyclonic anomaly at 40°–75°N over Eurasia beneath the anticyclone at 200 hPa. Overall this indicates a baroclinic initial structure (seen by the vertical variation in the streamfunction initial conditions), so that the amplifying block could draw upon the available potential energy of the extratropical optimal initial structure. The optimal initial OLR anomaly involves a broad region of enhanced OLR representing suppressed tropical convection from 140°E to 120°W, strongly resembling the Day_b −7 OLR composite.

The deterministic evolution from the 14-day optimal structure is calculated from (3) with Day_o 0 corresponding to the occurrence of the optimal initial structure, to be distinguished from the composite analysis

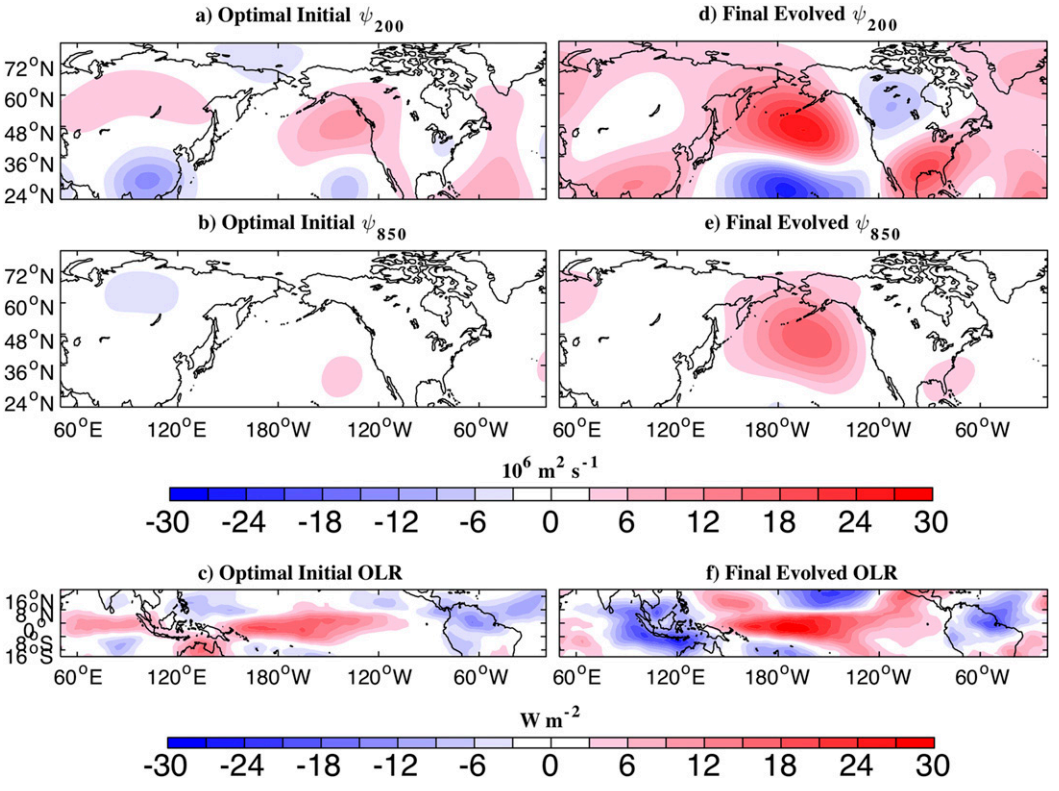

FIG. 8. The (a)–(c) optimal initial and (d)–(f) evolved final structures that most rapidly evolve into a central Pacific block in the LIM with a 14 day forecast lead time, for (top) 200 hPa extratropical streamfunction, (middle) 850 hPa extratropical streamfunction, and (bottom) tropical OLR.

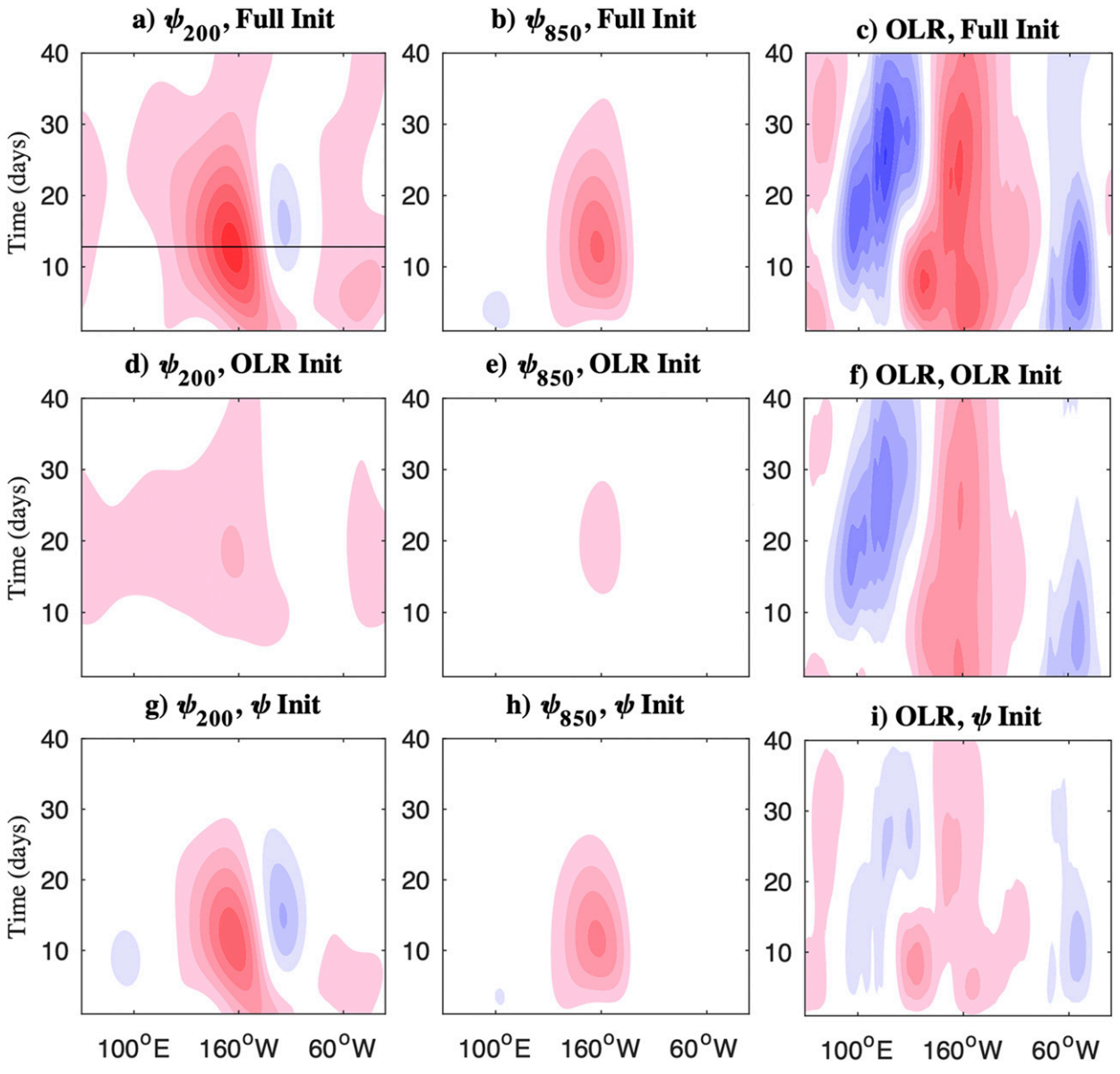

FIG. 9. Hovmöller diagrams of the LIM evolution of the optimal initial conditions shown in Fig. 7, for the evolution of (a)–(c) the full-state optimal initial structure, (d)–(f) the tropical OLR component of the optimal initial structure, and (g)–(i) the extratropical streamfunction component of the optimal initial structure. (left) 40°–60°N averaged 200 hPa extratropical streamfunction, (middle) 40°–60°N averaged 850 hPa extratropical streamfunction, and (right) 10°S–10°N averaged OLR. The *y* axis indicates the days following initialization of the 14-day optimal initial condition. The solid black line in (a) marks the time of peak block intensity (12 days following initialization).

(Figs. 1–5) where Day_b 0 indicates the day of block onset. The solid black lines in Figs. 5a and 9a indicate the time of peak amplitude for a more direct comparison of the composite-based and LIM-based block evolution. By Day_o +14, when blocking amplification has maximized via (9), the final evolved structure is largely equivalent barotropic and, not surprisingly, strongly resembles the target norm (cf. Figs. 8d,e and Figs. 6c,d). Although the optimal initial condition maximized growth over a 14-day period, the block became established by about Day_o +7, and persisted for two weeks after its peak on Day_o +12. The LIM evolution of the 200 hPa streamfunction optimal initial condition compares quite well with the observed composite evolution shown in Fig. 5a, relative to the peak intensity of the block. In particular, the LIM captures the observed westward retrogression of the east Pacific anticyclone, subsequent block amplification, downstream development of the trough over North America, and ridging in the North Atlantic.

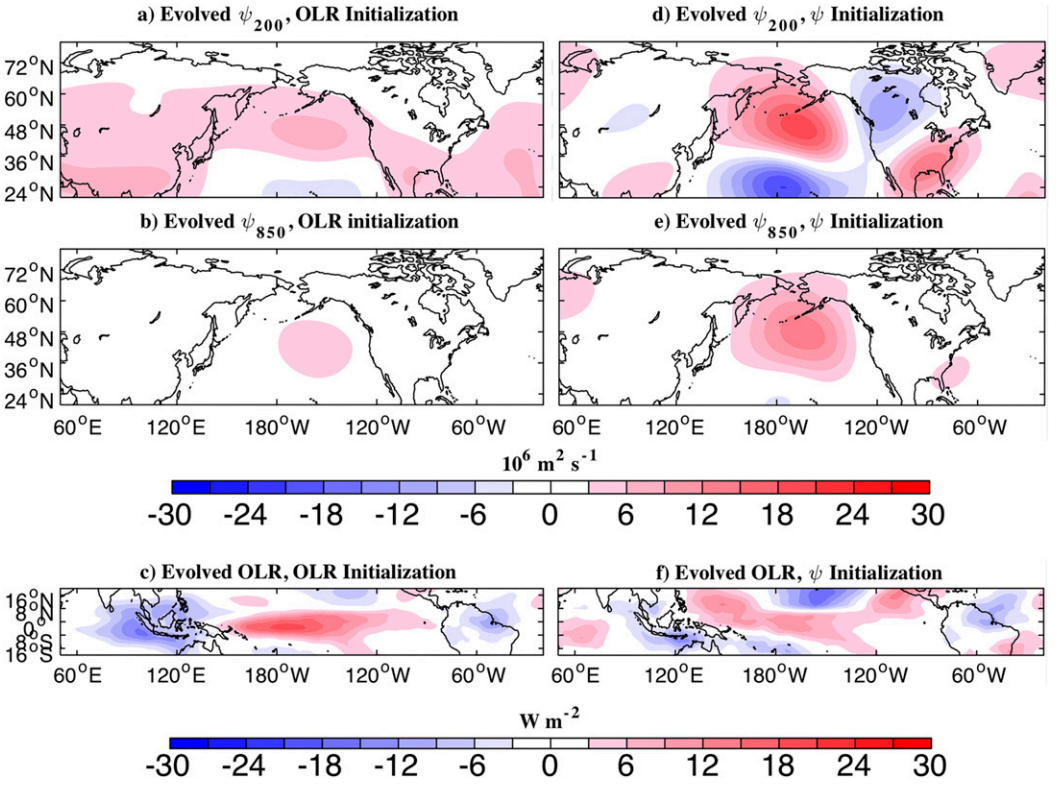

FIG. 10. The final evolved pattern in the LIM attained by initializing with only (a)–(c) the tropical OLR component of the optimal initial structure, and (d)–(f) the extratropical streamfunction component of the optimal initial structure, for a lead time of 14 days.

While tropical OLR is not used in defining the blocking norm, its evolution through (3) throughout the 14-day time interval, and its related interaction with the extratropical streamfunction, influenced development of the block. The positive OLR anomaly persisted through Day$_o$ +14, while a negative OLR anomaly developed at 80°E from Day$_o$ +5 to Day$_o$ +20, subsequently propagating eastward to 140°E from Day$_o$ +20 through Day$_o$ +35 (Figs. 8f and 9c). This tropical evolution is roughly consistent with the transition of the Madden–Julian oscillation from Phase 3 to 5 (Wheeler and Hendon 2004). The peak extratropical response to the tropical initial conditions from Day$_o$ +15 to Day$_o$ +20 coincides with the eastward propagation of the negative OLR anomaly, as it transitions from destructively to constructively interfering with the stationary negative OLR anomaly associated with La Niña conditions (Figs. 9d,f). A similar evolution was found under an L2 norm in Winkler et al. (2001).

c. *The relative roles of tropical and extratropical initial conditions in block development*

To isolate the influence of different components within the state vector on the LIM block evolution, we initialized the LIM with only the extratropical streamfunction (Figs. 8a,b) or only the tropical OLR portion (Fig. 8c) of the optimal initial structure, and then (3) was used to determine the subsequent Day$_o$ +14 evolved state. The optimal initial OLR structure alone can produce a troposphere-deep anticyclonic block in the central Pacific (Figs. 9e,d and 10a,b), but with notably reduced amplitude and overall slower growth compared to evolution from the full optimal. Furthermore, the 850 hPa streamfunction anticyclone is centered slightly farther to the south than its 200 hPa counterpart. A more zonal pattern is evident at 200 hPa, reminiscent of the leading L2 optimal (not shown but see Winkler et al. 2001). Likewise, the downstream trough over North America is no longer present, replaced by a broad anticyclonic anomaly over much of the continental United States.

Initializing the LIM with only the initial optimal streamfunction patterns yields an evolved quadrupole structure at 200 hPa, including an extratropical anticyclone in the central Pacific that contributes to the block by Day$_o$ +14 (Figs. 9g,h). The evolved structure is similar to the negative PNA, except for the location of the anticyclone over the southeastern United States which is centered farther to the west over the Gulf

states (cf. Fig. 10d, Fig. C1b). The subtropical cyclonic anomaly is centered west of Hawaii, which more closely matches the actual position of the cyclonic anomaly observed in the composite blocking pattern and in the norm (Figs. 1d and 6c). At 850 hPa an anticyclonic anomaly developed in the central Pacific whose intensity, shape, and location relative to its 200 hPa counterpart is indicative of a more equivalent barotropic structure than the evolved structure initialized from the optimal initial OLR. The 200 hPa streamfunction response to the initial streamfunction conditions peaked around Day$_o$ +10–15, representing a stronger but shorter-lived impact upon the extratropics and the initial extratropical structure, than the optimal initial tropical OLR conditions (cf. Fig. 9d, Fig. 9g).

The above results suggest that the full optimal evolution of blocking in the LIM may be characterized by a combination of an extratropics-induced, wavelike anomaly at shorter lead times and a tropics-induced ENSO-like response at longer lead times. While the 200 hPa anticyclonic anomaly produced by each component was similarly located in the central extratropical Pacific, the vertical structure of the block, subtropical cyclone anomaly location, and North American evolution all differed substantially. The net response produced a stronger central Pacific anticyclone (conducive to blocking), weaker trough over the western United States and stronger anticyclone over the southeastern United States.

d. Relationship between optimal growth and observed blocking events

In the previous section, we found optimal structures that *could* lead to maximum development of North Pacific blocking over a 14-day interval. Here, we test whether observed blocks *do* develop in this way. First, we compare the projection of observed anomalies onto the initial optimal structure (involving both OLR and extratropical streamfunction) with the projection of the observed anomalies 14 days later onto the blocking norm (involving only extratropical streamfunction), where the projection is computed as the dot product of the system state **x** with either the initial optimal structure, or the blocking norm, in PC space. The resulting scatterplot (Fig. 11a) shows a fairly linear relationship between the two projection time series, with a correlation of 0.66. (Note that, although in this paper we do not focus on the evolution of the oppositely signed pattern; by construction it too must evolve linearly via the LIM.) The positive relationship between the two shows that the optimal initial structure can predict the emergence of a blocked state at a 14-day lead; the amount of scatter is not necessarily surprising, since the noise in (2), which includes unpredictable nonlinearities in the system, also plays a role in the (unpredictable) development of blocks. When we instead compare the projection onto either the optimal initial streamfunction anomaly (Fig. 11b) or the optimal initial OLR anomaly

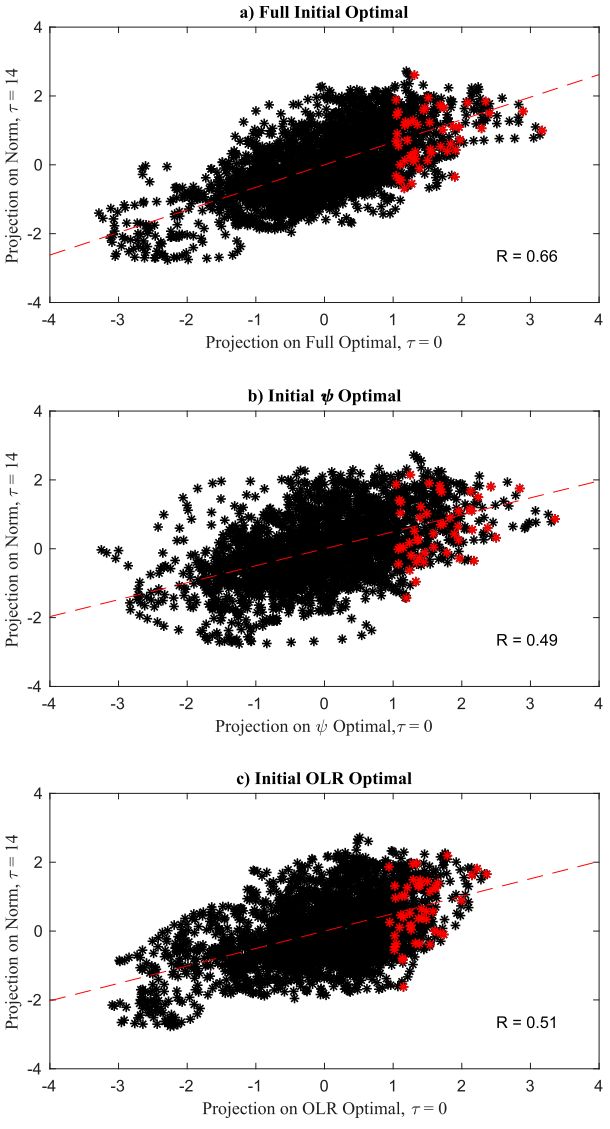

FIG. 11. Scatterplots of the strength of the projection of the reanalysis state onto (a) the full-state optimal initial structure, (b) the extratropical streamfunction optimal, and (c), the tropical OLR optimal, vs the strength of the projection of the reanalysis state onto the blocking norm 14 days later. Each black star represents this relationship for every day in the data record. The red lines indicate the linear fit to the data using a least squares approach, with slopes of (a) 0.66, (b) 0.49, and (c) 0.51. Red points indicate the top 50 optimal projections, that are separated by at least 14 days, that project most strongly onto the (a) full-state components of the initial optimal structure, (b) extratropical streamfunction, and (c) tropical OLR.

(Fig. 11c) with the projection onto the blocking norm at Day$_o$ +14, however, the correlation is substantially reduced. This demonstrates that the combined knowledge of both the tropical OLR state and the extratropical streamfunction state enhances the ability to anticipate a blocked state two weeks in advance.

Would knowledge of the initial optimal structure amplitude have been useful to anticipate the onset of the events used to construct the blocking composite? Table 2 shows the optimal initial projection amplitudes observed 14 days prior to each block onset, revealing that two weeks prior to block onset, 18 of the 21 blocking events were preceded by positive projection onto the optimal initial state, with nine having an initial amplitude greater than one standard deviation. That is, as also suggested by Fig. 11a, the likelihood of a block forming two weeks after a positive projection onto the optimal initial structure is notably enhanced.

The optimal initial structure defined by the LIM maximizes growth under the blocking norm, thereby representing a theoretical best-case scenario for blocking, but in general not all features of these patterns will always occur prior to each block's formation. Figures 12a–c show the composite of the 50 independent cases for which the initial optimal structure projected most strongly onto the state vector at Day$_o$ 0 (red stars Fig. 11a). The plots shown represent the evolution of the non-EOF truncated streamfunction and OLR anomalies, so this ''optimal composite'' may be compared to the blocking-onset composite in Figs. 1 and 2; the black lines again indicate significance at the 99% level using a two-tailed Student's t test. [Recall, however, that the blocking composite is defined by block *onset* whereas the optimal composite is defined by peak block *amplitude*.] Similar to the optimal initial pattern (Fig. 8a), the 200 hPa streamfunction optimal composite has an anticyclone in the east Pacific with a subtropical trough to its south (Fig. 12a). However, the trough over China in the initial optimal structure is *not* observed in the composite, which may indicate that this feature is more a result of due to the effects of EOF truncation on the LIM optimal structure. Other details in the initial composite generally match those in the optimal initial condition.

Fourteen days after a strong projection of the state onto the optimal initial structure is identified, the optimal composite contains a central Pacific block, although its amplitude is weaker than for the blocking-onset composite (Figs. 12d,e versus Figs. 1b,e), which is likely due to averaging over many more cases (i.e., spread in red stars along the y axis in Fig. 11a). Still, on average a more blocked state is observed to follow a positive projection onto the optimal initial structure. The cyclonic anomalies in the subtropical Pacific and over North America are notably weaker than the LIM-evolved block, and the block composite. These features were developed from the extratropical initial condition, suggesting that at 14 days the tropical initial condition is influencing the full-state optimal projection more than the extratropical initial condition. Given the higher-frequency variability of the extratropics, this result is not surprising but should be considered when attempting to predict blocking at subseasonal time scales. The reanalysis composite of tropical OLR remains characterized by positive OLR anomalies in the central Pacific at Day$_o$ +14, although the anomaly weakened over this period rather than strengthening as the optimal initial structure evolves in the LIM (Fig. 12f). A more sprawling region of negative OLR anomalies formed over the eastern Indian Ocean and Maritime Continent similar to that observed in the LIM.

TABLE 2. Correspondence between the blocking events identified to construct the norm, the projections onto the 14-day optimal initial patterns 14 days prior to block onset, and projection onto the blocking norm the day of block onset.

Date of block onset	Duration (days)	Projection onto optimal 14 days prior to block onset	Projection onto norm at block onset
17 Jan 1982	6	0.4329	1.4748
3 Feb 1982	10	0.9010	1.1658
20 Dec 1983	9	0.1407	1.1064
14 Jan 1984	8	1.1608	1.3956
1 Feb 1985	8	1.0555	1.6366
25 Dec 1988	6	1.2332	1.3200
31 Jan 1989	29	0.8549	1.5638
15 Dec 1990	17	0.9779	1.4101
23 Jan 1991	6	−0.9985	1.5638
17 Dec 1992	28	0.4815	1.2500
12 Feb 1994	8	0.9794	1.5182
21 Jan 1996	11	2.0374	1.6350
16 Feb 1996	11	−0.2083	1.4450
19 Dec 1998	8	1.0588	1.7756
12 Jan 2000	12	1.8078	2.2364
24 Dec 2004	18	−0.2400	1.1434
20 Feb 2007	7	0.3765	1.2795
21 Jan 2008	7	1.0722	1.5329
14 Feb 2009	15	0.0764	1.3672
15 Dec 2010	10	1.3523	1.1695
13 Feb 2011	16	1.7744	1.2782
Mean projection		0.7775	1.4413

5. Sensitivity to optimization time interval

For the 14-day optimization interval, both the tropics and extratropics affected blocking growth, and the corresponding block that developed persisted for roughly two weeks, weakening thereafter. However, the blocks identified in Table 1 had durations ranging from as

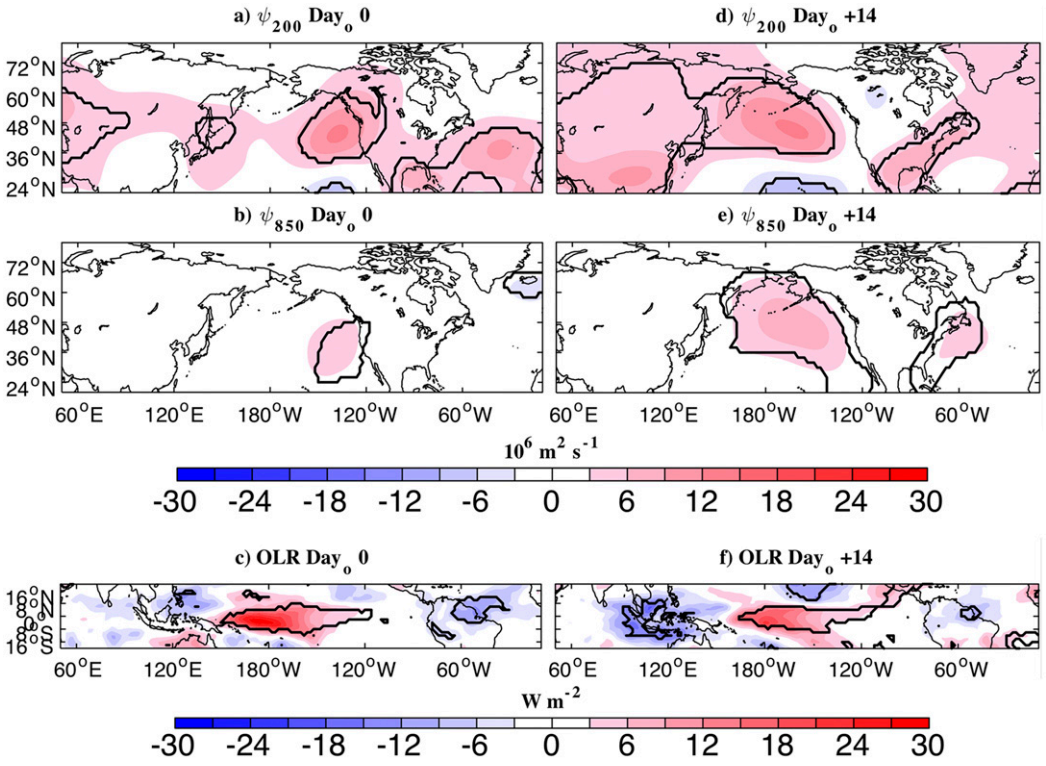

FIG. 12. Composite patterns for the 50 independent reanalysis dates that projected most strongly onto the full-state optimal initial structure. Composites are provided for (a)–(c) Day$_o$ 0, when the reanalysis state projected most strongly onto the initial optimal structure, and (d)–(f) Day$_o$ +14, when a blocked state is anticipated. Plots are provided for (top) 200 hPa extratropical streamfunction anomalies, (middle) 850 hPa extratropical streamfunction anomalies, and (bottom) tropical OLR anomalies. Black contours indicate where patterns are significant at the 99% level.

short as 6 days to as long as four weeks. One question that arises is whether each block's life cycle is associated with different contributions from the tropical and extratropical initial conditions. Therefore, we also determined the optimal structures for τ = 7- and 21-day time intervals. The strength of the block that developed for each optimization interval, using the full-state, tropical and extratropical initial conditions, was evaluated by projecting the evolved pattern at each day onto the blocking norm kernel (Figs. 6c,d) at each forecast lead time. The resulting time series provide a measure of the amplitude of the block as it evolves from the optimal initial conditions (Fig. 13).

Peak amplitude is similar using the 7- and 14-day optimals (Figs. 13a,b), while the block diminished more rapidly when evolved from the 7-day optimal. The downstream trough that developed from the 7-day optimal is stronger than the 14-day optimal, consistent with the stronger extratropics-induced pattern (cf. Fig. 14g, Fig. 9g). For a 21-day optimization lead time, however, the relative contributions from the tropics and extratropics were roughly equal, with the extratropics-induced amplification peaking a few days earlier than the tropics-induced amplification (cf. Fig. 13c; Fig. 15). Given substantial overlap between the tropical and extratropical contributions, the block maintained considerable amplitude from Day$_o$ +10 to Day$_o$ +30 (Figs. 15a,b). The downstream trough developed by the extratropical initial condition is much weaker than that observed in the composite block evolution and is negated by the influence of the tropical initial condition (Figs. 15a,d,g). The tropical OLR evolution in this case differed substantially from the 7-day optimization interval and evolved predominantly due to the tropical OLR initial condition (Figs. 15c,f,i).

6. Discussion and conclusions

In this study, we examined the spatial and temporal evolution of North Pacific blocking events in the NCEP Reanalysis, using composite analysis (in which no assumption of linearity is necessary) and using a LIM. We found that the LIM can reproduce most aspects of the

observed composite evolution, suggesting the processes that drive North Pacific block development on weekly time scales are, in part, predictable, and are either linear or can be parameterized as linear. We emphasize that nonlinear amplification can still contribute to block development via the noise forcing [see Eq. (2)], but this component of the evolution is not predictable on weekly time scales, nor is it necessary to produce a block. North Pacific blocks can amplify via linear, nonnormal interactions over a period up to four weeks, with growth maximized for a lead time of 10 days. The optimal precursors to blocking at a 14-day lead time included an upper-level east Pacific anticyclone and suppressed convection over the central tropical Pacific. The tropics and extratropics both contributed to the deterministic evolution of blocking, with the tropics acting on longer time scales but imposing a weaker response than that contributed by the extratropics. The tropical contribution was driven by La Niña–like conditions that produced a hemispheric anticyclonic anomaly, while the extratropical contribution resembled the PNA pattern but with some clear distinctions. In reanalysis, there is good correspondence between a high projection on the optimal initial conditions and a blocked state 14 days later. The relative contributions of the tropics and extratropics are sensitive to the optimization interval, so that extratropical blocks are largely internally driven, that is, driven by extratropical dynamics, at a 7-day lead time, but are equally affected by the tropics and extratropics by a 21-day lead time.

The LIM's ability to reproduce the observed blocking evolution suggests that blocking on weekly time scales is predictably linear (with a noise residual), which is equivalent to a nonlinear system where the nonlinearities act on time scales substantially faster than linear processes (Martinez-Villalobos et al. 2018). We note that our results are consistent with nonlinear dynamics that are predictable on synoptic time scales, just not weekly time scales, which could also include the "threshold" behavior suggested to initiate blocking by Nakamura and Huang (2018). While the primitive equations that dictate blocking development are indeed nonlinear, temporally course-graining these equations essentially averages out the details of nonlinearities that decorrelate rapidly compared to linearities (Hasselmann 1976). Additionally, from the quasigeostrophic potential vorticity (q) perspective the low-frequency q tendency, dq'/dt, is proportional to the *temporal average* (over at least several days) of the high-frequency, nonlinear q flux convergence $\nabla \cdot \overline{\mathbf{v}''q''}$ in the absence of sources and sinks D

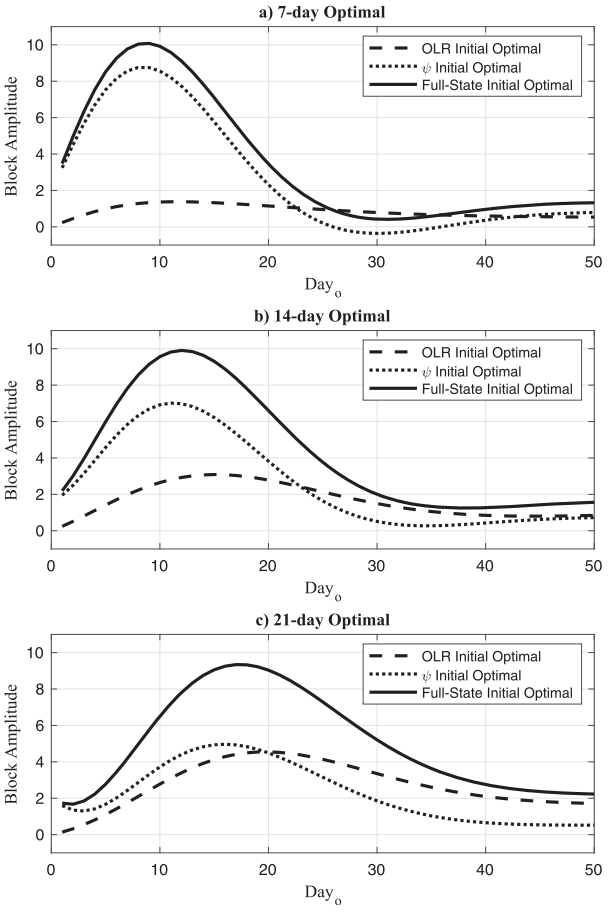

FIG. 13. Time series of the block amplitude as a function of lead time, achieved by propagating (a) the 7-day optimal initial conditions, (b) 14-day optimal initial conditions, and (c) 21-day optimal initial conditions forward in time. The solid curves show the amplification using the full-state initial condition, the dotted curves using the extratropical streamfunction initial condition, and the dashed curves using the tropical OLR initial condition, for each optimization interval.

$$\frac{dq'}{dt} + \nabla \cdot \overline{\mathbf{v}''q''} = D \tag{12}$$

(Hoskins et al. 1983). Thus the 7-day-averaged anomalies upon which the LIM is based implicitly include the atmospheric response to the aggregate effect of high-frequency nonlinearities. This eddy–mean interaction is the basis under which Shutts (1983) postulated that blocks could be maintained in regions of strong deformation.

Our results provide additional evidence, through an independent and novel approach, for several preexisting blocking theories:

1) role of deformation associated with blocking as suggested by Shutts (1983);
2) teleconnections and the impact of tropical heating on blocking (Renwick and Wallace 1996); and

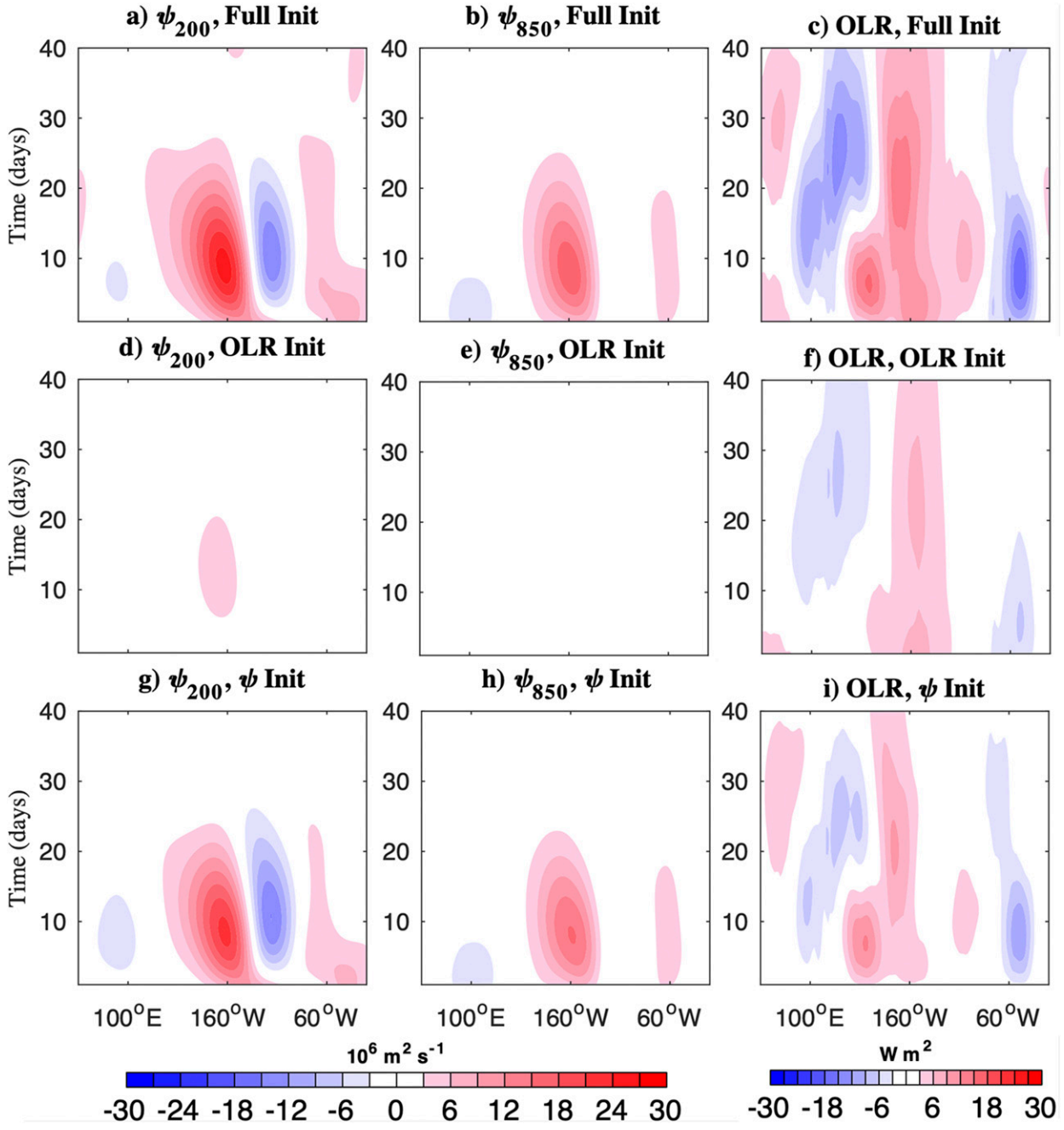

FIG. 14. As in Fig. 9, but for the 7-day optimal initial condition.

3) baroclinic and nonmodal processes in North Pacific block amplification (Evans and Black 2003; Breeden and Martin 2018).

The east Pacific anticyclone observed in the 14-day optimal retrograded and amplified in the central Pacific to produce a block. Considering the Shutts perspective, it is possible that the high-frequency synoptic forcing, $\mathbf{v}''q''$, (where double-primed notation represents high-frequencyanomalies with respect to the long-term mean) which maintains the low-frequency block via eddy straining is, in part, a linear function of the block amplitude,$\mathbf{v}''q'' \sim Tq'$ (where T is a scalar quantity and the single prime $'$ denotes low-frequency anomalies), a relationship which could be captured in the dynamic operator $\mathbf{L}$. Breeden and Martin (2018) also found, using piecewise potential vorticity inversion,

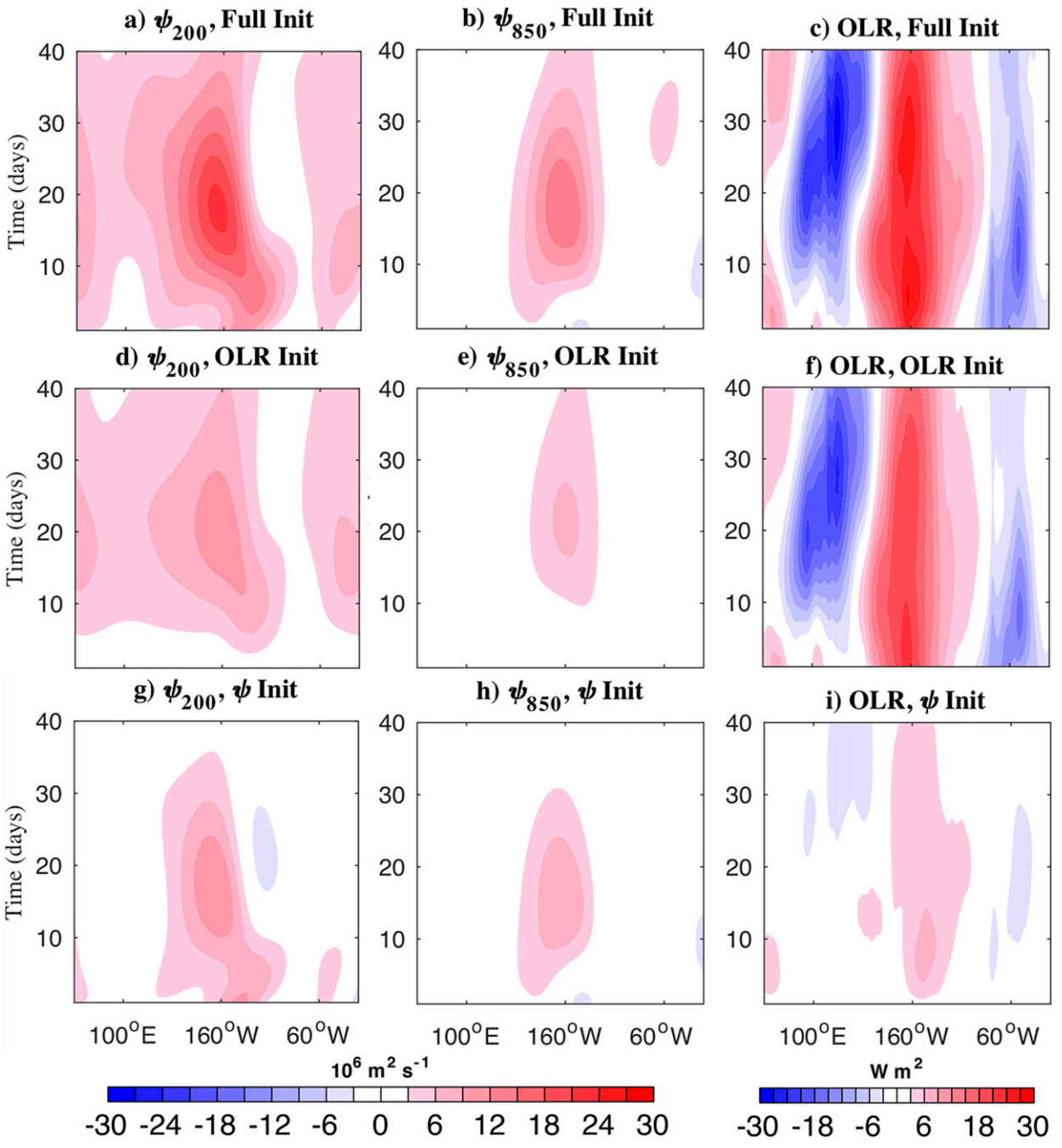

FIG. 15. As in Fig. 9, but for the 21-day optimal initial condition.

that deformation (a linear term from this perspective) contributed to the amplification of a North Pacific block in late February 2006, whose evolution closely matches that simulated by the LIM.

The contribution of the optimal initial tropical OLR conditions that produce blocking found in this study provides further evidence for the impact of anomalous tropical heating and divergence on the circulation of the extratropical atmosphere (Sardeshmukh and Hoskins 1988) and specifically blocking (Renwick and Wallace 1996). Our results indicate that the tropics-induced extratropical response amplifies the pattern associated with internal extratropical interactions, whose dynamics as represented by $\mathbf{L}$ are independent of ENSO phase. That is, internal extratropical dynamics and tropically coupled dynamics both drive blocking independently

of each other and may be treated additively. Still, it would be interesting to test whether the dynamics themselves are a strong function of ENSO phase, by constructing new LIMs based on La Niña or El Niño conditions alone. The MJO teleconnection to blocking was not clear in this study. While a propagating feature on the time scales of the MJO was observed in the LIM evolution of tropical heating from the optimal initial condition (Fig. 9c), this occurred after the block had developed, not before. However, it is possible that the MJO variance is muted or obscured by the dominance of ENSO in the model, or that the simulated evolution involves periods of constructive and destructive interference between MJO and ENSO-related heating as discussed by Winkler et al. (2001). Future work will employ a LIM decoupled from ENSO dynamics to better distinguish MJO and ENSO-related teleconnections and their effect on blocking.

Extratropical teleconnections were also found to develop as part of the block, both in reanalysis and in the LIM. The PNA pattern was produced by evolving the extratropical optimal initial condition, consistent with the results of Cash and Lee (2001). Franzke et al. (2011) performed a synoptic analysis of the PNA and found a similar precursor east Pacific anticyclone eight days prior to its negative phase. The PNA alone did not, however, fully explain the evolved pattern from the extratropical initial condition, most notable over North America where the trough–ridge pattern was shifted northwest of that associated with the pure PNA (cf. Fig. 10d, Fig. C1b). These differences indicate that the PNA interacted with other portions of the atmospheric state to produce the blocking pattern. Motivated by the connection between east and central Pacific blocking, we investigated the optimal initial conditions leading to an *east* Pacific anticyclone in the LIM for a 14-day lead time but found only weak anomaly growth (not shown).

In the context of the LIM, this suggests that the east Pacific precursor may develop largely through unpredictable noise forcing, which implies limited prospects for predicting both the east Pacific precursor and, thereafter, its subsequent central Pacific block development.

The baroclinicity of the optimal initial extratropical streamfunction pattern, which evolved into an equivalent barotropic block, provides additional evidence for the linear baroclinic processes that Evans and Black (2003) and Breeden and Martin (2018) found to heavily contribute to North Pacific block amplification. Breeden and Martin (2018) also isolated the nonmodal, or transient, contribution to blocking amplification, and found that as the vertical structure of height anomalies

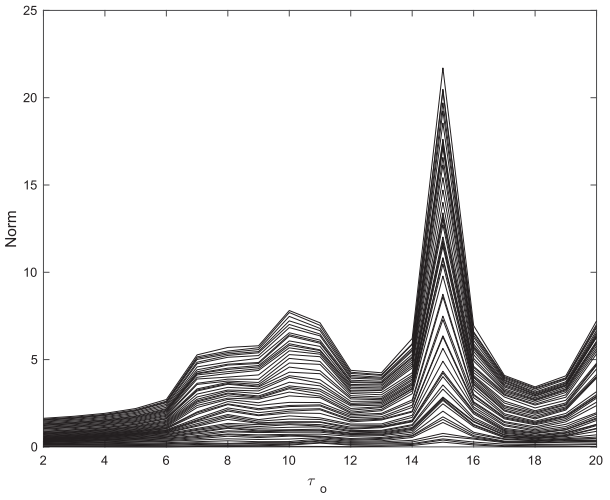

FIG. A1. Tau test for the linear inverse model as in Penland and Sardeshmukh (1995). Values of the norm of the submatrices of the dynamical operator $\mathbf{L}$ are plotted against the τ_o used to compute the lagged covariance matrix. Each line represents the norm of the submatrices that compose $\mathbf{L}$, so for $\mathbf{L}$ with $N \times N$ dimensions, the norm is determined for $\mathbf{L}(1, 1)$, $\mathbf{L}(1{:}2, 1{:}2)$, $\mathbf{L}(1{:}3, 1{:}3)$ etc., through $\mathbf{L}(1{:}N, 1{:}N)$.

transitioned from having a westward tilt with height to an equivalent barotropic structure, the nonmodal term steadily contributed to block amplification. Given the transition of the baroclinic 14-day optimal which was baroclinic, to the equivalent barotropic block produced by the LIM (Fig. 8), the LIM may be reproducing the effect noted in Breeden and Martin (2018).

The optimal structures for the growth of central Pacific blocking in our LIM are consistent with the results of previous observational analyses of North Pacific blocking. Jaffe et al. (2011) examined the composite evolution of North Pacific jet retractions, which similarly are associated with a dipole-type block, finding structures at the tropopause preceding retraction onset that bear a striking resemblance to the optimal initial structure for central Pacific blocking identified by the LIM, including the east Pacific ridge. They also observed a statistically significant zonally elongated anticyclonic anomaly over eastern Russia/China, poleward of the jet entrance region prior to retraction, similar to the anticyclonic anomaly in the optimal (Fig. 8a). Breeden and Martin (2018, 2019) performed a case study of a jet retraction and highlighted the importance of a Eurasian anticyclone that encountered the poleward side of the jet entrance region, inducing waves that weakened the jet via the aggregate effect of nonlinear processes over a 5-day period, consistent with the eddy–mean interaction represented by (12). The subsequent evolution involved the development of a high-amplitude ridge that reinforced a preexisting block,

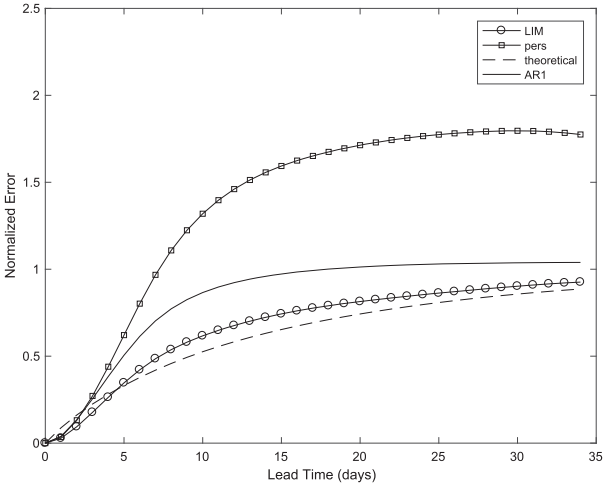

FIG. B1. Change in error variance with changing forecast lead time predicted by theory (black dash), produced by the LIM (open circles), an AR(1) process (solid black), and persistent (open squares).

which may explain the role of the Eurasian anticyclonic anomaly observed in the 14-day optimal initial structure.

The inherent time scales of blocking development might limit their predictability for forecast leads of 2–6 weeks. However, knowledge of the initial optimal conditions can serve as a guide for knowing which features could lead to a regime shift as represented by these blocks, which in turn could also degrade forecast skill (Winters et al. 2019). Albers and Newman (2019) demonstrated that a LIM can be used to predict the skill of subseasonal forecasts a priori, presenting a method to distinguish periods when these forecasts may or may not be useful. This approach could be used to determine when blocking may develop versus when the signal-to-noise ratio is too high to have confidence in the forecast. The LIM approach can also be used to interrogate numerical weather prediction (NWP) errors in blocking prediction, by comparing a LIM derived from lagged analyses with a LIM derived from the equivalent lagged analysis in NWP forecasts. Differences in the LIM and optimal initial structures that produce observed errors in NWP blocking prediction is anticipated as a follow-on study from this work. Finally, we acknowledge that the impact of variables not included in our simple state vector could, of course, change the growth characteristics of blocking; expanding this simple model to include more information, such as a tropical ocean (e.g., ENSO) or stratospheric component, could be an avenue of future work.

Acknowledgments. The authors appreciate funding for this project which was supplied through the NOAA Climate Program Office Modeling, Analysis, Predictions and Projections (MAPP) Program. The authors would also like to thank Professors Michael Morgan and Stephanie Henderson for their insightful comments

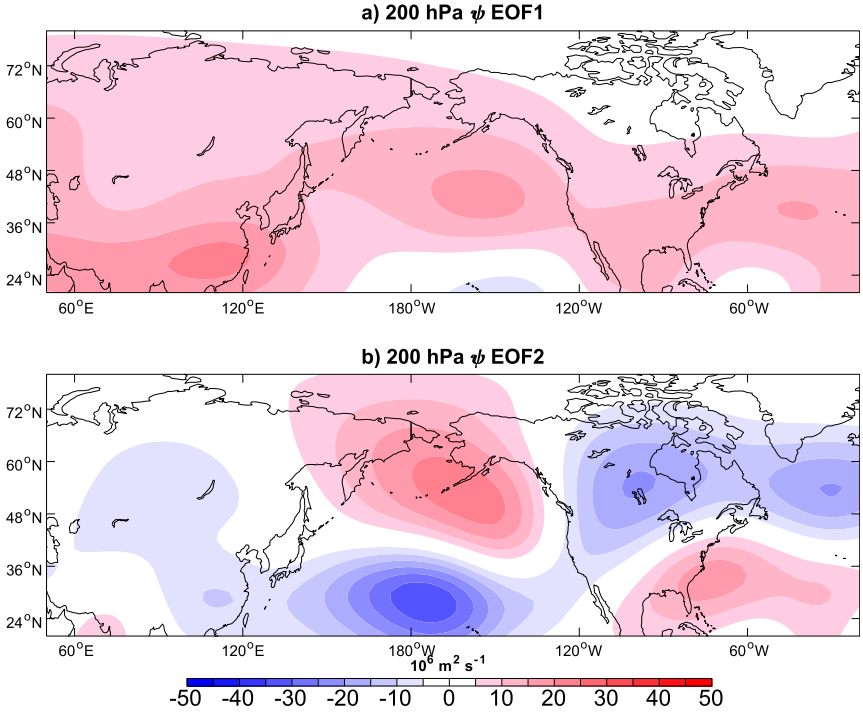

FIG. C1. (a) EOF1 and (b) EOF2 patterns of 200 hPa streamfunction.

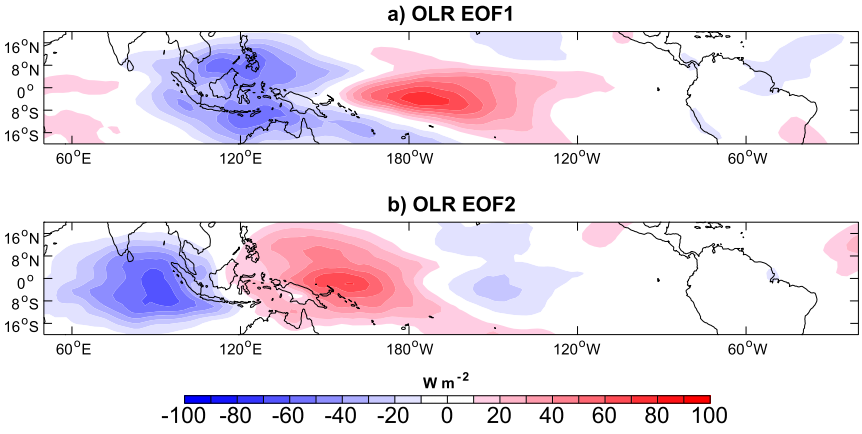

FIG. C2. (a) EOF1 and (b) EOF2 patterns of tropical OLR.

during the course of this study, as well as the comments from two anonymous reviewers.

APPENDIX A

Test for Linear Dynamics

To determine whether the dynamical system operator is independent of the lag used to define it, the tau test after Penland and Sardeshmukh (1995) is employed. If the system was perfectly linear, any time period used to calculate the lagged covariance and dynamic operator would produce the same results. In reality this is not the case, given the sensitivity of the dynamics to lags that are half of the period of the normal modes of the system, referred to as a Nyquist period (Penland and Sardeshmukh 1995). It is therefore important to verify that the lag used to develop the LIM is not unduly affected by proximity to time scales of the underlying eigenmodes, and is within the range at which the lag does not significantly alter the estimate of $\mathbf{L}$. To this end, $\mathbf{L}$ is calculated using varying lags, and the Euclidean norms of $\mathbf{L}$ and its submatrices are then computed. When the norms of the submatrices are constant with varying optimization time τ_o, the dynamics of the system as represented by $\mathbf{L}$ are independent of the τ_o chosen to define it. The norm of $\mathbf{L}$ in this model is shown in Fig. A1 for a range of optimization lead times. The results suggest that a lag of six days or less would be appropriate for calculating $\mathbf{L}$.

APPENDIX B

Error Growth

Another test for the LIM is whether error in the model evolves in a manner consistent with theory. Penland (1989) demonstrated that the global error $\delta(\tau)$ should equal the trace of the error covariance matrix:

$$\langle \mathbf{e}(\tau)\mathbf{e}(\tau)^{\mathrm{T}} \rangle = \mathbf{C}(0) - \mathbf{G}(\tau)\mathbf{C}(0)\mathbf{G}^{\mathrm{T}}(\tau).$$

Figure B1 shows the observed error in the LIM compared with error predicted by theory, a persistence forecast, and a forecast treating the system as a first-order autoregressive [AR(1)] process. While the observed error in the LIM is slightly higher than theory predicts, it is lower than both persistence and AR(1) by a substantial amount. The error growth overall follows the behavior expected under a stable, linear system forced by stochastic noise.

APPENDIX C

Leading EOFs of the State Vector Variables

For reference we include the two leading modes of variability for 200 hPa streamfunction (Fig. C1) and tropical OLR (Fig. C2), to compare with the patterns observed under the blocking norm.

REFERENCES

Adams, J., and P. Swarztrauber, 1997: SPHEREPACK 2.0: A model development facility. NCAR Tech. Note NCAR/TN-436+STR, NCAR, https://doi.org/10.5065/D6Z899CF.

Albers, J. R., and M. Newman, 2019: A priori identification of skillful extratropical subseasonal forecasts. *Geophys. Res. Lett.*, **46**, 12 527–12 536, https://doi.org/10.1029/2019GL085270.

Barcilon, A., and C. H. Bishop, 1998: Nonmodal development of baroclinic waves undergoing horizontal shear deformation. *J. Atmos. Sci.*, **55**, 3583–3597, https://doi.org/10.1175/1520-0469(1998)055<3583:NDOBWU>2.0.CO;2.

Barnes, E. A., J. Slingo, and T. Woollings, 2012: A methodology for the comparison of blocking climatologies across indices,

models and climate scenarios. *Climate Dyn.*, **38**, 2467–2481, https://doi.org/10.1007/s00382-011-1243-6.

Barnston, A. G., and R. E. Livezey, 1987: Classification, seasonality, and persistence of low-frequency atmospheric circulation patterns. *Mon. Wea. Rev.*, **115**, 1083–1126, https://doi.org/10.1175/1520-0493(1987)115<1083:CSAPOL>2.0.CO;2.

Berggren, R., B. Bolin, and C.-G. Rossby, 1949: An aerological study of zonal motion, its perturbations and break-down. *Tellus*, **1**, 14–37, https://doi.org/10.3402/tellusa.v1i2.8501.

Borges, M. D., and P. D. Sardeshmukh, 1995: Barotropic Rossby wave dynamics of zonally varying upper-level flows during northern winter. *J. Atmos. Sci.*, **52**, 3779–3796, https://doi.org/10.1175/1520-0469(1995)052<3779:BRWDOZ>2.0.CO;2.

Breeden, M., and J. E. Martin, 2018: Analysis of the initiation of an extreme North Pacific jet retraction during boreal winter. *Quart. J. Roy. Meteor. Soc.*, **144**, 1895–1913, https://doi.org/10.1002/qj.3388.

——, and ——, 2019: Evidence for nonlinear processes in fostering a North Pacific jet retraction. *Quart. J. Roy. Meteor. Soc.*, **145**, 1559–1570, https://doi.org/10.1002/qj.3512.

Campetella, C., and M. Rusticucci, 1998: Synoptic analysis of an extreme heat wave over Argentina in March 1980. *Meteor. Appl.*, **5**, 217–226, https://doi.org/10.1017/S1350482798000851.

Carrera, M. L., R. W. Higgins, and V. E. Kousky, 2004: Downstream weather impacts associated with atmospheric blocking over the northeast Pacific. *J. Climate*, **17**, 4823–4839, https://doi.org/10.1175/JCLI-3237.1.

Cash, B. A., and S. Lee, 2001: Observed nonmodal growth of the Pacific–North American teleconnection pattern. *J. Climate*, **14**, 1017–1028, https://doi.org/10.1175/1520-0442(2001)014<1017:ONGOTP>2.0.CO;2.

Chiang, J. C. H., and D. J. Vimont, 2004: Analogous meridional modes of atmosphere–ocean variability in the tropical Pacific and tropical Atlantic. *J. Climate*, **17**, 4143–4158, https://doi.org/10.1175/JCLI4953.1.

Dole, R., and N. D. Gordon, 1983: Persistent anomalies of the extratropical Northern Hemisphere wintertime circulation: Geographical distribution and regional persistence characteristics. *Mon. Wea. Rev.*, **111**, 1567–1586, https://doi.org/10.1175/1520-0493(1983)111<1567:PAOTEN>2.0.CO;2.

——, and Coauthors, 2011: Was there a basis for anticipating the 2010 Russian heat wave? *Geophys. Res. Lett.*, **38**, L06702, https://doi.org/10.1029/2010GL046582.

Evans, K. J., and R. X. Black, 2003: Piecewise tendency diagnosis of weather regime transitions. *J. Atmos. Sci.*, **60**, 1941–1959, https://doi.org/10.1175/1520-0469(2003)060<1941:PTDOWR>2.0.CO;2.

Farrell, B. F., 1984: Modal and nonmodal baroclinic waves. *J. Atmos. Sci.*, **41**, 668–673, https://doi.org/10.1175/1520-0469(1984)041<0668:MANMBW>2.0.CO;2.

Farrell, B., 1988: Optimal excitation of neutral Rossby waves. *J. Atmos. Sci.*, **45**, 163–172, https://doi.org/10.1175/1520-0469(1988)045<0163:OEONRW>2.0.CO;2.

——, and P. J. Ioannou, 1993: Stochastic dynamics of baroclinic waves. *J. Atmos. Sci.*, **50**, 4044–4057, https://doi.org/10.1175/1520-0469(1993)050<4044:SDOBW>2.0.CO;2.

Franzke, C., S. B. Feldstein, and S. Lee, 2011: Synoptic analysis of the Pacific–North American teleconnection pattern. *Quart. J. Roy. Meteor. Soc.*, **137**, 329–346, https://doi.org/10.1002/qj.768.

Frederiksen, J. S., 1998: Precursors to blocking anomalies: The tangent linear and inverse problems. *J. Atmos. Sci.*, **55**, 2419–2436, https://doi.org/10.1175/1520-0469(1998)055<2419:PTBATT>2.0.CO;2.

Hasselmann, K., 1976: Stochastic climate models Part I. Theory. *Tellus*, **6**, 473–485, https://doi.org/10.1111/j.2153-3490.1976.tb00696.x.

Henderson, S. A., E. D. Maloney, and E. A. Barnes, 2016: The influence of the Madden–Julian oscillation on Northern Hemisphere winter blocking. *J. Climate*, **29**, 4597–4616, https://doi.org/10.1175/JCLI-D-15-0502.1.

——, ——, and S.-W. Son, 2017: Madden–Julian oscillation Pacific teleconnections: The impact of the basic state and MJO representation in general circulation models. *J. Climate*, **30**, 4567–4587, https://doi.org/10.1175/JCLI-D-16-0789.1.

Hoskins, B. J., I. N. James, and G. H. White, 1983: The shape, propagation and mean-flow interaction of large-scale weather systems. *J. Atmos. Sci.*, **40**, 1595–1612, https://doi.org/10.1175/1520-0469(1983)040<1595:TSPAMF>2.0.CO;2.

Jaffe, S. C., J. E. Martin, D. J. Vimont, and D. J. Lorenz, 2011: A synoptic-climatology of episodic, sub-seasonal retractions of the Pacific jet. *J. Climate*, **24**, 2846–2860, https://doi.org/10.1175/2010JCLI3995.1.

Kalnay, E., and Coauthors, 1996: The NCEP/NCAR 40-Year Reanalysis Project. *Bull. Amer. Meteor. Soc.*, **77**, 437–471, https://doi.org/10.1175/1520-0477(1996)077<0437:TNYRP>2.0.CO;2.

Lau, W. K. M., and K.-M. Kim, 2012: The 2010 Pakistan flood and Russian heat wave: Teleconnection of hydrometeorological extremes. *J. Hydrometeor.*, **13**, 392–403, https://doi.org/10.1175/JHM-D-11-016.1.

Liebmann, B., and C. A. Smith, 1996: Description of a complete (interpolated) outgoing longwave radiation dataset. *Bull. Amer. Meteor. Soc.*, **77**, 1275–1277.

Martinez-Villalobos, C., D. J. Vimont, C. Penland, M. Newman, and J. D. Neelin, 2018: Calculating state-dependent noise in a linear inverse model framework. *J. Atmos. Sci.*, **75**, 479–496, https://doi.org/10.1175/JAS-D-17-0235.1.

Matsueda, M., 2011: Predictability of Euro-Russian blocking in summer of 2010. *Geophys. Res. Lett.*, **38**, L06801, https://doi.org/10.1029/2010GL046557.

Miller, R. L., G. M. Lackmann, and W. A. Robinson, 2020: A New Variable-Threshold Persistent Anomaly Index: Northern Hemisphere Anomalies in the ERA-Interim Reanalysis. *Mon. Wea. Rev.*, **148**, 43–62, https://doi.org/10.1175/MWR-D-19-0144.1.

Mu, M., and Z. N. Jiang, 2008: A method to find perturbations that trigger blocking onset: Conditional nonlinear optimal perturbations. *J. Atmos. Sci.*, **65**, 3935–3946, https://doi.org/10.1175/2008JAS2621.1.

Nakamura, N., and C. S. Y. Huang, 2018: Atmospheric blocking as a traffic jam in the jet stream. *Science*, **361**, 42–47, https://doi.org/10.1126/science.aat0721.

Otkin, J. A., and J. E. Martin, 2004: The large-scale modulation of subtropical cyclogenesis in the central and eastern Pacific Ocean. *Mon. Wea. Rev.*, **132**, 1813–1828, https://doi.org/10.1175/1520-0493(2004)132<1813:TLMOSC>2.0.CO;2.

Parker, T. J., G. J. Berry, and M. J. Reeder, 2014: The structure and evolution of heat waves in southeastern Australia. *J. Climate*, **27**, 5768–5785, https://doi.org/10.1175/JCLI-D-13-00740.1.

Pelly, J. L., and B. J. Hoskins, 2003: A new perspective on blocking. *J. Atmos. Sci.*, **60**, 743–755, https://doi.org/10.1175/1520-0469(2003)060<0743:ANPOB>2.0.CO;2.

Penland, C., 1989: Random forcing and forecasting using principal oscillation pattern analysis. *Mon. Wea. Rev.*, **117**, 2165–2185, https://doi.org/10.1175/1520-0493(1989)117<2165:RFAFUP>2.0.CO;2.

——, and P. D. Sardeshmukh, 1995: The optimal growth of tropical sea surface temperature anomalies. *J. Climate*, **8**, 1999–2024, https://doi.org/10.1175/1520-0442(1995)008<1999:TOGOTS>2.0.CO;2.

Renwick, J. A., and J. M. Wallace, 1996: Relationships between North Pacific wintertime blocking, El Niño, and the PNA pattern. *Mon. Wea. Rev.*, **124**, 2017–2076, https://doi.org/10.1175/1520-0493(1996)124<2071:RBNPWB>2.0.co;2.

Rex, D. F., 1950: Blocking action in the middle troposphere and its effect upon regional climate. *Tellus*, **2**, 196–211, https://doi.org/10.1111/j.2153-3490.1950.tb00331.x.

Röthlisberger, M., S. Pfahl, and O. Martius, 2016: Regional-scale jet waviness modulates the occurrence of mid-latitude weather extremes. *Geophys. Res. Lett.*, **43**, 10 989–10 997, https://doi.org/10.1002/2016GL070944.

Sardeshmukh, P. D., and B. J. Hoskins, 1988: The generation of global rotational flow by steady idealized tropical divergence. *J. Atmos. Sci.*, **45**, 1228–1251, https://doi.org/10.1175/1520-0469(1988)045<1228:TGOGRF>2.0.CO;2.

——, G. P. Compo, and C. Penland, 2015: Need for caution in interpreting extreme weather statistics. *J. Climate*, **28**, 9166–9187, https://doi.org/10.1175/JCLI-D-15-0020.1.

Shutts, G. J., 1983: The propagation of eddies in diffluent jetstreams: Eddy vorticity forcing of "blocking" flow fields. *Quart. J. Roy. Meteor. Soc.*, **109**, 737–761, https://doi.org/10.1002/qj.49710946204.

Tibaldi, S., and F. Molteni, 1990: On the operational predictability of blocking. *Tellus*, **42A**, 343–365, https://doi.org/10.3402/tellusa.v42i3.11882.

Tziperman, E., and P. Ioannou, 2002: Transient growth and optimal excitation of thermohaline variability. *J. Phys. Oceanogr.*, **32**, 3427–3435, https://doi.org/10.1175/1520-0485(2002)032<3427:TGAOEO>2.0.CO;2.

Vimont, D. J., 2012: Analysis of the Atlantic meridional mode using linear inverse modeling: Seasonality and regional influences. *J. Climate*, **25**, 1194–1212, https://doi.org/10.1175/JCLI-D-11-00012.1.

——, M. A. Alexander, and M. Newman, 2014: Optimal growth of Central and East Pacific ENSO events. *Geophys. Res. Lett.*, **41**, 4027–4034, https://doi.org/10.1002/2014GL059997.

Wallace, J. M., and D. S. Gutzler, 1981: Teleconnections in the geopotential height field during the Northern Hemisphere winter. *Mon. Wea. Rev.*, **109**, 784–812, https://doi.org/10.1175/1520-0493(1981)109<0784:TITGHF>2.0.CO;2.

Wheeler, M. C., and H. H. Hendon, 2004: An all-season real-time multivariate MJO index: Development of an index for monitoring and prediction. *Mon. Wea. Rev.*, **132**, 1917–1932, https://doi.org/10.1175/1520-0493(2004)132<1917:AARMMI>2.0.CO;2.

Winkler, C. R., M. Newman, and P. D. Sardeshmukh, 2001: A linear model of wintertime low-frequency variability. Part I: Formulation and forecast skill. *J. Climate*, **14**, 4474–4494, https://doi.org/10.1175/1520-0442(2001)014<4474:ALMOWL>2.0.CO;2.

Winters, A. C., D. Keyser, and L. F. Bosart, 2019: The development of the North Pacific jet phase diagram as an objective tool to monitor the state and forecast skill of the upper-tropospheric flow pattern. *Wea. Forecasting*, **34**, 199–219, https://doi.org/10.1175/WAF-D-18-0106.1.

Yamazaki, A., and H. Itoh, 2013: Vortex–vortex interactions for the maintenance of blocking. Part I: The selective absorption mechanism and a case study. *J. Atmos. Sci.*, **70**, 725–742, https://doi.org/10.1175/JAS-D-11-0295.1.

Zanna, L., and E. Tziperman, 2005: Nonnormal amplification of the thermohaline circulation. *J. Phys. Oceanogr.*, **35**, 1593–1605, https://doi.org/10.1175/JPO2777.1.